Observational Estimates of Turbulent Mixing in the Southeast Indian Ocean

AJITHA CYRIAC,[a,b] HELEN E. PHILLIPS,[a,c] NATHANIEL L. BINDOFF,[a,c,d,e] HUABIN MAO,[f] AND MING FENG[g,h]

[a] *Institute for Marine and Antarctic Studies, University of Tasmania, Hobart, Tasmania, Australia*
[b] *ARC Centre of Excellence for Climate System Science, Hobart, Tasmania, Australia*
[c] *Australian Antarctic Program Partnership, Institute for Marine and Antarctic Studies, University of Tasmania, Hobart, Australia*
[d] *CSIRO Marine and Atmospheric Research, Hobart, Tasmania, Australia*
[e] *ARC Centre of Excellence in Climate Extremes, Hobart, Australia*
[f] *State Key Laboratory of Tropical Oceanography, South China Sea Institute of Oceanology, Chinese Academy of Sciences, Guangzhou, China*
[g] *CSIRO Oceans and Atmosphere, IOMRC, Crawley, Western Australia, Australia*
[h] *Centre for Southern Hemisphere Oceans Research, Hobart, Tasmania, Australia*

(Manuscript received 12 February 2020, in final form 7 April 2021)

ABSTRACT: This study investigates the spatiotemporal variability of turbulent mixing in the eastern south Indian Ocean using a collection of data from electromagnetic autonomous profiling explorer (EM-APEX) profiling floats, shipboard CTD, and microstructure profilers. The floats collected 1566 profiles of temperature, salinity, and horizontal velocity data down to 1200 m over a period of about four months. A finescale parameterization is applied to the float and CTD data to estimate turbulent mixing. Elevated mixing is observed in the upper ocean, over bottom topography, and in mesoscale eddies. Mixing is enhanced in the anticyclonic eddies due to trapped near-inertial waves within the eddy. We found that cyclonic eddies contribute to turbulent mixing in the depth range of 500–1000 m, which is associated with downward-propagating internal waves. The mean diapycnal diffusivity over 250–500-m depth is $O(10^{-6})$ $m^2 s^{-1}$, and it increases to $O(10^{-5})$ $m^2 s^{-1}$ in 500–1000 m in cyclonic eddies. The turbulent mixing in this region has implications for water-mass transformation and large-scale circulation. Higher diffusivity [$O(10^{-5})$ m^2 s^{-1}] is observed in the Antarctic Intermediate Water (AAIW) layer in cyclonic eddies, whereas weak diffusivity is observed in the Subantarctic Mode Water (SAMW) layer [$O(10^{-6})$ $m^2 s^{-1}$]. Counterintuitively, then, the SAMW water-mass properties are strongly affected in cyclonic eddies, whereas the AAIW layer is less affected. Comparatively high diffusivity at the location of the South Indian Countercurrent (SICC) jets suggests there are wave–mean flow interactions in addition to the wave–eddy interactions that warrant further investigation.

KEYWORDS: Internal waves; Mixing; Ocean circulation

1. Introduction

Turbulent mixing plays an important role in large-scale oceanic processes such as water-mass transformation, global overturning circulation, and stratification. It also distributes heat, salt, chemicals, and organisms throughout the world oceans. By distributing the energy input from winds and tides, turbulent mixing closes the oceanic energy budget (Bryan 1987; Wunsch and Ferrari 2004). Turbulence is the final stage of the energy cascade in the ocean where kinetic energy from winds and tides is transformed into molecular heat by viscosity (St. Laurent et al. 2012).

In the interior of the ocean, most of the mixing is attributed to the breaking of internal waves, which act as a bridge between the large-scale forcing and the molecular-scale dissipation (St. Laurent et al. 2012). Internal waves are generated mainly by fluctuating wind stress (D'Asaro 1985), tidal flow over steep topography (Egbert and Ray 2000), and geostrophic flow over rough topography (Nikurashin and Ferrari 2010). Near the ocean surface, the wind energy generates internal waves with near-inertial frequency that dominate the internal wave energy spectrum (Wunsch and Ferrari 2004). From a global study using Argo floats between 30° and 45°N, Whalen et al. (2018) found that the amplitude of turbulent mixing increases with increasing wind energy at the surface. They also found that the internal wave-driven mixing is strong in regions of anticyclonic vorticity compared to cyclonic vorticity regions. This is in agreement with the modification of wind-generated internal waves by anticyclonic eddies (Kunze 1985; Lee and Niiler 1998). The sensitivity of ocean models to the spatial and temporal variability of mixing has implications on ocean heat uptake in climate models (e.g., Harrison and Hallberg 2008) and ocean circulation in regional models (e.g., Benthuysen et al. 2014).

The intermittent and patchy nature of turbulence makes it difficult to measure from limited ship-based observations. By using a range of inverse models and finescale parameterization, Huussen et al. (2012) found that too little internal wave dissipation is available in the deep Indian Ocean to sustain the meridional overturning circulation since most of the internal wave energy is dissipated in the upper 1000 m. Waterhouse et al. (2014) combined a range of measurements from different

Denotes content that is immediately available upon publication as open access.

Supplemental information related to this paper is available at the Journals Online website: https://doi.org/10.1175/JPO-D-20-0036.s1.

Corresponding author: Ajitha Cyriac, ajitha.cyriac@utas.edu.au

DOI: 10.1175/JPO-D-20-0036.1

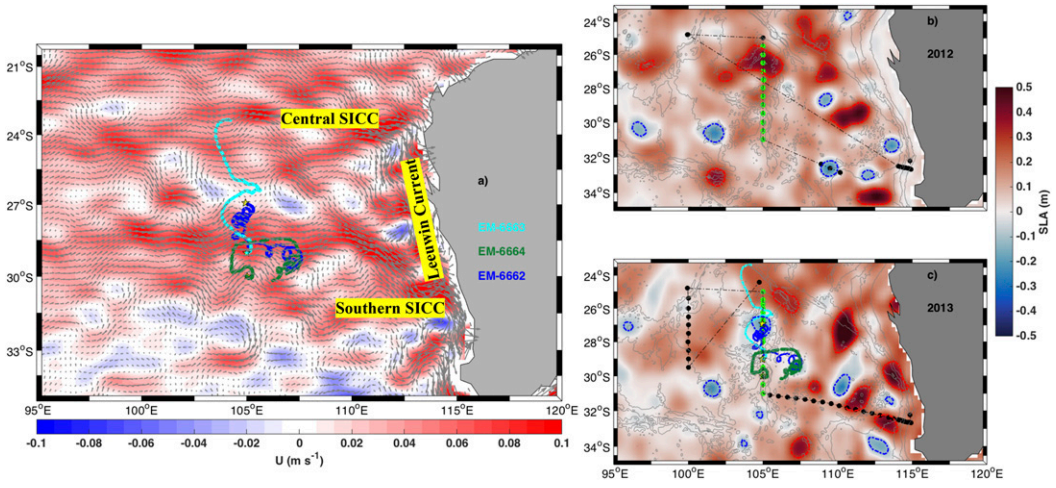

FIG. 1. (a) The tracks of EM-6662 (blue line), EM-6663 (cyan line), and EM-6664 (green line) are plotted over the eastward component of the mean geostrophic current (shading) during 2004–15 from AVISO. Arrows show the mean magnitude and direction of the flow. The different branches of the SICC and the Leeuwin Current are marked. Yellow stars represent the location of each float deployment. (b) Voyage track in 2012 and (c) voyage track in 2013. The light green stars in (b) and (c) are the microstructure profiler deployment locations. Background is the mean sea level anomaly during the microstructure measurements with bathymetry contours overlaid (200, 1000, 2000, 4000, 5000 m). Closed sea surface height contours of −0.1 (blue) and 0.3 m (red) show cyclonic and anticyclonic eddies, respectively.

instruments and calculated a global average diapycnal diffusivity of $O(10^{-5})$ m^2 s^{-1} above 1000-m depth and $O(10^{-4})$ m^2 s^{-1} below 1000-m depth with higher values in the abyssal ocean. They reported relatively low depth-averaged diffusivity [$O(10^{-6})$ m^2 s^{-1}] in the upper 1000 m of the eastern Indian Ocean. Using a strain-only parameterization, Whalen et al. (2012) reported an average diapycnal diffusivity of $O(10^{-5})$ m^2 s^{-1} over 250–500 m of the upper eastern south Indian Ocean. They observed elevated dissipation rates in regions of high eddy kinetic energy.

The surface circulation in the subtropical south Indian Ocean is characterized by the eastward flowing near surface geostrophic South Indian Countercurrent (SICC) (Siedler et al. 2006; Palastanga et al. 2007; Divakaran and Brassington 2011; Menezes et al. 2014). The SICC splits into different branches (Fig. 1) that become stronger and deeper as they approach the west coast of Australia (Divakaran and Brassington 2011). These branches act as a source of water for the poleward-flowing Leeuwin Current (LC) (Divakaran and Brassington 2011; Domingues et al. 2007; Menezes et al. 2013, 2014; Furue et al. 2017). The LC is accompanied by the subsurface Leeuwin Undercurrent (LUC), which flows equatorward underneath and just offshore of the LC (Thompson 1987; Furue et al. 2017). Unlike other eastern basins, the eastern south Indian Ocean (SIO) is found to be a region of high seasonal and interannual mesoscale variability (Birol and Morrow 2001). It possesses one of the highest eddy kinetic energy (EKE) bands in the World Ocean between 15° and 30°S (Jia et al. 2011). The mesoscale eddies generated from instabilities of the LC (Feng et al. 2005) and LUC (Rennie et al. 2007), as well as semiannual Rossby waves emanating from the eastern boundary (Morrow and Birol 1998), contribute to the observed variability over this region. These waves and eddies travel westward (Morrow et al. 2004) and interact with the SICC (Siedler et al. 2006). The subtropical south Indian Ocean is also a region of strong surface heat loss. In the seasonal cycle, the mixed layer heat storage in this region is primarily influenced by surface net heat flux and secondarily by turbulent entrainment (Cyriac et al. 2019).

Due to lack of enough observations, the turbulent mixing and the factors that influence it in the southeast Indian Ocean are not well described. In this study, we use microstructure measurements to validate the estimates of turbulent mixing from electromagnetic autonomous profiling explorer (EM-APEX) floats and shipboard CTD. We then investigate the variability of turbulent mixing in the southeast Indian Ocean, a region dominated by mesoscale eddies. We analyze the spatial and temporal variability of turbulent mixing and investigate its sources and implications for the first time in this climatically important region.

The paper is organized as follows: Section 2 describes the different datasets used in this study. The method of finescale parameterization used to estimate turbulent mixing from floats and shipboard data is explained in section 3. Section 4 describes the regional ocean characteristics observed from the floats and the shipboard data. The spatial and temporal variability of turbulent mixing in the upper 1000 m is analyzed in section 5. Section 6 investigates the factors influencing the observed mixing distribution. In section 7, we compare the different datasets and discuss the implications of mixing on water masses and large-scale circulation. Section 8 provides a summary of the present study.

2. Data

a. Shipboard data

Observations used in this study were collected from two voyages of the Marine National Facility (MNF) R/V *Southern*

TABLE 1. Deployment information of all the floats deployed in 2013 along 105°E.

Float	6664	6663	6218	6662	6217
Deployment date	10 Jul 2013	11 Jul 2013	12 Jul 2013	12 Jul 2013	13 Jul 2013
Date of last profile	25 Oct 2013	23 Oct 2013	2 Oct 2013	12 Oct 2013	5 Oct 2013
Latitude range	28.4°–30.1°S	23.3°–29.0°S	28.0°–31.7°S	26.9°–29.7°S	23.4°–28.4°S
Longitude range	104.2°–107.5°E	103.5°–105.6°E	103.7°–105.2°E	104.3°–107.6°E	104.9°–108.5°E
Depth (dbar)	1200	1200	300	1200	300
No. of profiles	520	518	1058	528	1102

Surveyor. The Voyage IN2012_V04 in 2012 consisted of 30 sampling stations at which CTD and lowered ADCP (LADCP) measurements were made (Fig. 1b). A Sea-Bird SBE911 CTD fitted in a rosette with 19 Niskin bottles, measured ocean temperature, salinity, dissolved oxygen, and pressure down to a depth of about 2000 m. Due to engine failure, research time was substantially reduced and CTD profiles were limited to the upper 2000 m.

The voyage SS2013_V04 in 2013 consisted of 58 sampling stations (Fig. 1c). The Sea-Bird SBE911 CTD fitted in a 19 bottle rosette frame, measured full-depth profiles of ocean temperature, salinity, dissolved oxygen, and pressure. During the 2013 voyage, five EM-APEX floats were deployed at various stations along 105°E (Fig. 1c, Table 1). In this study we use measurements from CTD data along the 105°E transect in 2012 and 2013 as well as three EM-APEX floats that profiled down to 1200 m.

In both years, CTD processing provided vertical profiles of temperature, salinity, and pressure at every 2 dbar. Due to LADCP instrument problems on both voyages, only a few of the velocity profiles were useful. We also used the shipboard measured wind data, corrected to 10-m winds to estimate friction velocity. (The data processing report for the shipboard underway, hydrographic, and velocity data is available at https://www.cmar.csiro.au/data/trawler.)

b. EM-APEX floats

The primary data used for this study are collected from three EM-APEX floats deployed in the southeast Indian Ocean in July 2013 along 105°E. They profiled until October 2013 between 23° and 32°S. EM-APEX floats are enhanced Argo floats that provide inexpensive high-resolution measurements of horizontal velocity in addition to the standard temperature, salinity, and pressure measurements. These floats use motional induction to measure the ocean velocity relative to a depth-independent reference velocity by measuring the electric current generated due to the movement of ocean water across the magnetic field of Earth (Sanford et al. 2005). The depth-independent reference velocity is determined from the surface GPS positions, following Phillips and Bindoff (2014). Two independent sets of electrodes measured the electric fields induced by the movement of the float (Sanford et al. 1978), providing two independent measurements of horizontal velocity. Vertical spacing of velocity samples is 3–4 dbar. The temperature, salinity, and pressure measurements at every 2–3 dbar are obtained from a Sea-Bird Electronics SBE-41 CTD. The temperature, salinity, and velocity were interpolated into a uniform pressure grid of 3 dbar before analysis. More details of the float data processing are provided in the appendix.

c. Microstructure

In this study, we use upper-ocean microstructure measurements of the turbulent dissipation of kinetic energy to provide confidence in the shear-strain parameterization used with the EM-APEX float data. The instrument used is a Rockland Scientific Vertical Microstructure Profiler (VMP) 200, an internally recording tethered profiler. The VMP measurements were taken during R/V *Southern Surveyor* voyages in 2012 (12 stations) and 2013 (18 stations) (Figs. 1b,c). At each CTD station along 105°E, in both 2012 and 2013, we measured turbulent dissipation to 300 m depth with a fall rate of 70 cm s^{-1}. The velocity shear probes collect the signals in frequency of 1250 Hz, which means the vertical scale of signal interval reach $O(1)$ mm. Here we calculate the dissipation rate at every 8 s and with 4-s overlap. The buoyancy frequency is calculated in the same depth interval in which the dissipation rate is calculated.

Each time the VMP was deployed, we positioned it at the sea surface and then allowed it to free fall to the limit of the 400-m neutrally buoyant line, which was run through a free-running block on the stern A-frame of the ship. We allowed a few minutes for the instrument to complete its descent once the rope was fully extended and then hauled the VMP back to the surface. Three such profiles were completed at each station that were then averaged to get the final profile for each station. During the cast, the ship was moving slowly ahead at 0.5–1 knot (kt; 1 kt $\approx$ 0.51 m s^{-1}) to keep the VMP away from the propellers. Thus, the depth range of the instrument was limited to approximately 300 m. The VMP200 sensors included one temperature and two shear probes. The data were processed using the ocean data assimilation system (ODAS) Matlab toolbox.

d. Auxiliary data

For the eastern SIO, the TropFlux wind product performed best in a recent comparison with moored flux measurements (Cyriac et al. 2019). However, since TropFlux is limited to north of 30°S and some of the float profiles are south of 30°S, we used the National Centers for Environmental Prediction (NCEP) wind product to have a full record. The hourly wind stress data are obtained from the NCEP Climate Forecast System, version 2 (Kanamitsu et al. 2002). It is a fully coupled model in which the interaction between atmosphere, ocean, land, and sea ice is incorporated. These hourly data have a

spatial resolution of 0.5° × 0.5°. We use the ETOPO1 (Amante and Eakins 2009) bathymetry data with a 1-arc-min (0.01° × 0.01°) spatial resolution. The daily sea level anomaly (SLA) and absolute surface geostrophic velocities were obtained from Copernicus Marine Environment Monitoring Service (CMEMS) on a 0.25° × 0.25° spatial grid (https://cds.climate.copernicus.eu). The float tracks are analyzed using the SLA and relative vorticity maps to identify float profiles associated with mesoscale eddies. A TOPEX/Poseidon 7.2 (TPXO7.2) global tidal model that uses the Laplace tidal equations and along-track altimeter data from TOPEX/Poseidon satellites is used to estimate the depth-averaged barotropic currents from the eight primary (M_2, S_2, N_2, K_2, K_1, O_1, P_1, Q_1) harmonic tidal constituents.

3. Methods

a. Dissipation rate of turbulent kinetic energy

1) Shear-strain parameterization

In a stationary and homogeneous internal wave field, the rate of energy transfer from large scales to small scales is assumed to be equal to the turbulent dissipation rate (ε) due to internal wave breaking (Gregg et al. 2003; Polzin et al. 2014). Finescale parameterization, which operates on a vertical wavelength range that transfers energy between these scales, connects the turbulent dissipation at smaller scales to nonlinearity in the internal wave field (Polzin et al. 2014). This method parameterizes the turbulent dissipation rate from shear (velocity) and strain (density) variances of the internal waves using internal wave–wave interaction theories (McComas and Muller 1981; Henyey et al. 1986). It parameterizes the net effects of shear and strain in transporting energy associated with high-frequency waves to dissipation scales (Polzin et al. 2014). There are two major assumptions for this parameterization: 1) most of the mixing in the ocean interior is due to internal wave breaking, and 2) the energy cascade due to nonlinear interactions of internal waves results in energy dissipation (Waterman et al. 2013; Whalen et al. 2015). Since it is easier to obtain velocity and density measurements in the finescale than microstructure observations, finescale parameterization is frequently used to estimate the turbulent dissipation rate (Polzin et al. 2014).

With these assumptions, the dissipation rate of turbulent kinetic energy can be written as (Gregg 1989; Polzin et al. 2002; Garabato et al. 2004; Meyer et al. 2015)

$$\varepsilon = \varepsilon_0 \left(\frac{N^2}{N_0^2}\right) \frac{\langle V_z^2\rangle^2}{\langle V_{z\text{-GM}}^2\rangle^2} \left(\frac{f}{f_0}\right) \frac{\cosh^{-1}(N/f)}{\cosh^{-1}(N_0/f_0)} \frac{3(R_\omega+1)}{2R_\omega\sqrt{2(R_\omega-1)}}, \tag{1}$$

where $\varepsilon_0 = 8 \times 10^{-10}\,\mathrm{W\,kg^{-1}}$, $N_0 = 3$ cph, $f_0 = 7.836 \times 10^{-5}\,\mathrm{s^{-1}}$, N is the local buoyancy frequency, and f is the local inertial frequency. Here $\langle V_z^2\rangle$ is the vertical shear variance normalized by N and $\langle V_{z\text{-GM}}^2\rangle$ is the corresponding shear variance predicted by Garrett and Munk (GM76; Cairns and Williams 1976) model. The angle brackets denote the wavenumber range over which the shear and strain variances are integrated. The range of integration varies from minimum wavenumber to a cutoff value above which the nonlinear effects lead to wave breaking (Polzin et al. 2014). The spectrum is integrated from a vertical wavenumber of 0.0026 cpm^{-1} (383 m) to the high wavenumber limit (cutoff wavenumber m_c) where integrated shear variance reaches $2\pi N^2/10$ (Polzin et al. 2014; Figs. 2a,b). When the estimated cutoff wavenumber exceeds the limit of the spectrum, we set it to 25 m, a reasonable limit up to which the nonlinear effects are less important (Fig. 2).

The shear-strain ratio R_ω is the ratio of horizontal kinetic energy to potential energy for a single wave frequency averaged over a single internal wave's phase (Polzin et al. 2002, 2014). It can be written as

$$R_\omega = \frac{\langle V_z^2\rangle}{\langle \xi_z^2\rangle}, \tag{2}$$

where $\langle V_z^2\rangle$ is the vertical shear variance normalized by N. Here ξ_z is the strain, derived as $\xi_z = (N^2 - \langle N_{\mathrm{ref}}^2\rangle)/\langle N_{\mathrm{ref}}^2\rangle$ where $\langle N_{\mathrm{ref}}^2\rangle$ is the mean squared buoyancy frequency. The local buoyancy frequency, $N^2 = -(g/\rho_0)(\partial\rho_\theta/\partial z)$, is estimated using the adiabatic levelling method (Bray and Fofonoff 1981). Here ρ_θ is the potential density relative to the sea surface calculated from the EM-APEX salinity, temperature, and pressure profiles. The density gradient is estimated from a linear regression between density and pressure over a vertical pressure window of 6 dbar. The mean squared buoyancy frequency $\langle N_{\mathrm{ref}}^2\rangle$ is calculated as a moving average of 40 consecutive profiles of buoyancy frequency estimated over a longer pressure window of 24 m where $\langle\,\rangle$ represents the horizontal averaging. Ideally, it should be a time mean of many profiles measured at each location (Polzin et al. 2014). But since the floats are not stationary, the mean profile is calculated this way.

Low R_ω values at high vertical wavenumber indicate the presence of high-frequency internal waves, whereas a decreasing ratio with wavenumber indicates the dominance of near-inertial waves (Polzin et al. 2002). In the ocean interior, R_ω generally varies from 5 to 20 (Polzin et al. 1995; Chinn et al. 2016). Under the single wave approximation, the intrinsic frequency of the wave can be written as $\omega = f\sqrt{(R_\omega+1)/(R_\omega-1)}$ where f is the inertial frequency (e.g., Polzin et al. 1995).

To determine the direction of propagation of the internal waves, we have used the ratio of counterclockwise (CCW) to clockwise (CW) shear variance (polarization ratio) (Leaman and Sanford 1975). A dominance of the CCW polarized shear indicates downward energy propagation with upward phase propagation, whereas a dominance of CW polarized shear indicates upward energy propagation with downward phase propagation in the Southern Hemisphere.

In this study, we use the Mixing (MX) Oceanographic Toolbox for EM-APEX data (Meyer et al. 2014), which combines finescale parameterization of turbulent dissipation rate from both shear and strain methods using hydrographic and velocity data. The dissipation rate and diffusivity from EM-APEX floats and shipboard data are estimated using the toolbox. In the toolbox, the transfer function was corrected to be quadratic in the shear variance calculation so that the spectra will roll-off with a slope of m^{-1} at higher wavenumbers where m is the vertical wavenumber (Fig. 2a). We also changed the input pressure window for the calculation of potential density gradient from 6 to 3 dbar in the

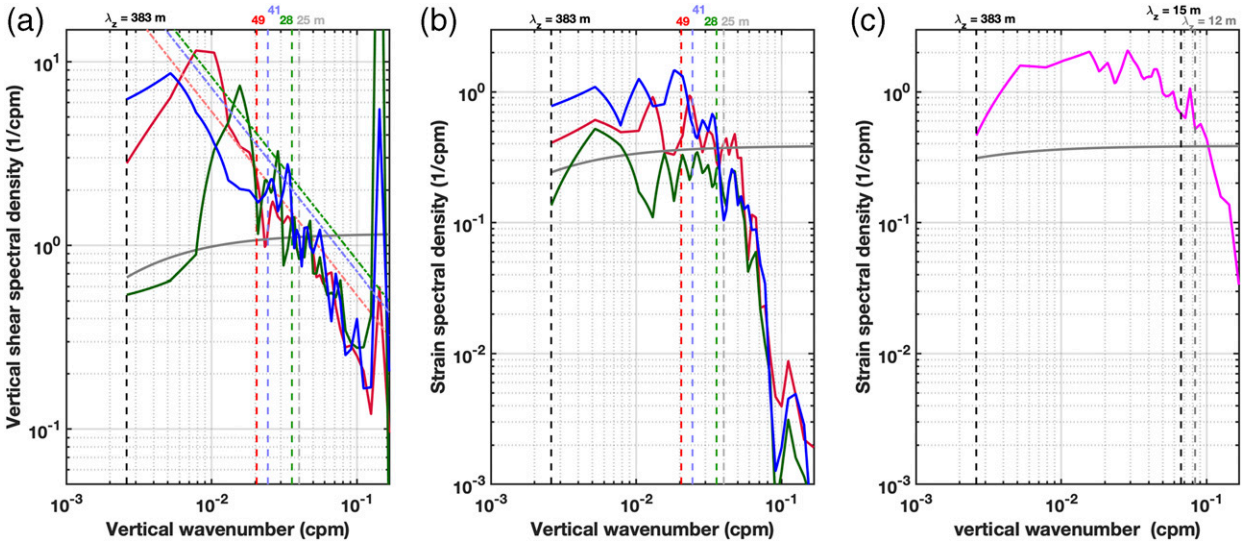

FIG. 2. Mean (a) buoyancy scaled shear spectra and (b) strain spectra for a typical profile from EM-6662 (red), EM-6663 (green), and EM-6664 (blue). The vertical colored dashed lines are the corresponding cutoff wavenumbers m_c, calculated from each spectrum [section 3a(1)]. The dashed colored slanted lines on the shear spectra represent the m_c/m roll-off for each spectrum. (c) The mean strain spectrum of a typical shipboard CTD profile. In all the panels, the solid gray lines are the corresponding Garrett and Munk (GM) spectra. In (c), the vertical black dashed lines represent the range of vertical wavenumbers of integration. In all cases, 383 m is the wavelength of the minimum wavenumber limit of integration and 25 (12) m (vertical gray dashed line) is the wavelength of the maximum vertical wavenumber permitted for the integration for the float (shipboard CTD) data to avoid including higher wavenumber noise.

calculation of N^2, based on the temperature and salinity gradient vertical wavenumber spectra for the float data. Moreover, we set the cutoff wavenumber for strain spectrum to be equal to the limit identified in the corresponding shear spectrum of each profile to avoid integrating into the instrument noise of the strain spectrum (K. Polzin 2020, personal communication). We also changed the default cutoff wavenumber for shear and strain spectra in the toolbox from 12 to 25 m. This is because, when we used 12 m, we found that in about 276 profiles out of 1566 profiles (17%), the strain spectrum was integrated into the instrument roll-off region that is an artifact of the measurement technique rather than due to internal waves (Fig. 2). Further, we tested the sensitivity of the mixing estimates to the choice of integration limits by setting a constant high wavenumber limit corresponding to a wavelength of 50 m. Even though the magnitude of the mixing estimates changed, the spatial patterns along the float tracks remained the same and the conclusions are robust to the choice of high wavenumber limit.

2) FINESCALE STRAIN PARAMETERIZATION

Strain-based parameterization has been used to estimate mixing in regional (e.g., Sloyan 2005) and global studies (e.g., Whalen et al. 2012, 2015, 2018), where strain-based estimates have been found to agree with microstructure measurements within a factor of 2–3 in the open ocean. This method is very effective when only the strain (density) information is available. Here we apply the strain parameterization to CTD data collected from the ship.

The dissipation rate for the strain-only parameterization can be written as

$$\varepsilon = \varepsilon_0 \left(\frac{N^2}{N_0^2}\right) \frac{\langle \xi_z^2 \rangle^2}{\langle \xi_{z\text{-GM}}^2 \rangle^2} h(R_\omega) L(f, N), \tag{3}$$

where $\xi^2_{z\text{-GM}}$ is the GM76 strain variance, $h(R_\omega)$ describes the dependence on shear–strain ratio and $L(f, N)$ is a latitudinal correction (Polzin et al. 1995; Gregg et al. 2003). R_ω is set to 6 based on the R_ω estimates from the EM-APEX profiles that are close in space and time (within 10–30 km and about one day) to the CTD measurements. Following Whalen et al. (2012, 2015), we removed buoyancy frequency values larger than $5 \times 10^{-4}\,\mathrm{s}^{-2}$ to avoid large buoyancy jumps at the base of the mixed layer, setting these to missing values. We also removed N^2 less than $10^{-9}\,\mathrm{s}^{-2}$. Following the float data, the strain spectrum is integrated from a vertical wavenumber of 0.0026 cpm^{-1} (383 m) to the high wavenumber limit where integrated strain variance reaches $2\pi N^2/10$ (Fig. 2c) or 12 m, using whichever is larger.

3) MICROSTRUCTURE MEASUREMENTS

The dissipation rate of turbulent kinetic energy ε can be estimated from the VMP measurements of vertical shear $\partial u/\partial z$ as

$$\epsilon = \frac{15}{2} \nu \overline{\left(\frac{\partial u}{\partial z}\right)^2} = \frac{15}{2} \nu \int_0^{k_{\max}} \psi(k)\, dk, \tag{4}$$

where ν is the kinematic viscosity calculated from temperature, salinity, and density measurements, the overline indicates a spatial average, u is either one of the two horizontal components of velocity, z is the vertical coordinate, $\psi(k)$ is the spectrum of the vertical shear, and k is the vertical wavenumber (Osborn 1980). The upper limit of integration $k_{\max}$ is variable. Following Shang et al. (2017),

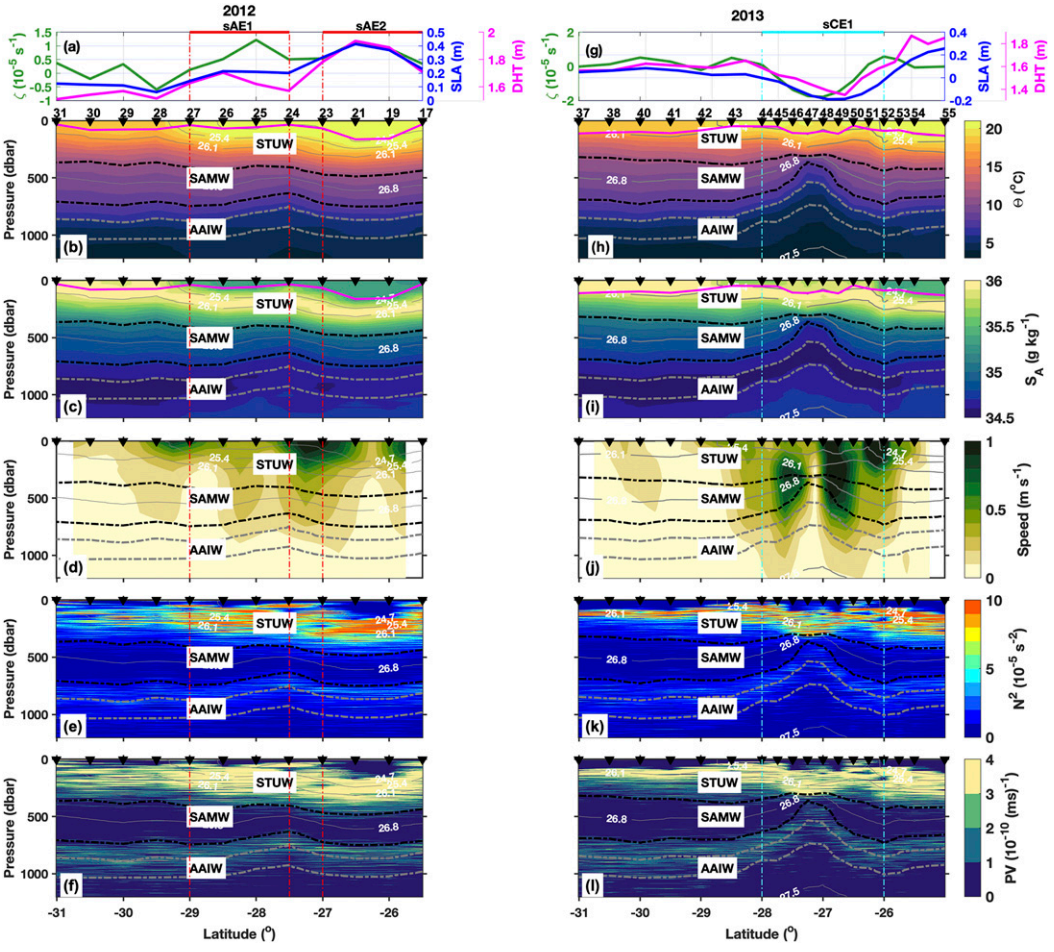

FIG. 3. The meridional variation of (a) SLA (blue), relative vorticity (green) and DHT (100/1500 dbar, pink), (b) Conservative Temperature, (c) Absolute Salinity, (d) geostrophic speed, (e) buoyancy frequency, and (f) potential vorticity (ζ term is ignored; see section 3c) for shipboard observations in 2012. The light gray lines are potential density relative to the sea surface with an interval of 0.7 kg m^{-3}. (g)–(l) As in (a)–(f), but for 2013. Station numbers are marked at the top of Conservative Temperature (b) and (h). The heavy gray contours in all panels show the potential density range of AAIW (27.1–27.3 kg m^{-3}), and heavy black lines show SAMW (26.7–26.9 kg m^{-3}). The STUW is the high salinity near-surface water. In 2012, there were two anticyclonic eddies (sAE1 and sAE2) and a cyclonic eddy (sCE1) in 2013. Mixed layer depth along the ship tracks is marked over temperature and salinity (magenta line). The horizontal extent of each cyclonic (anticyclonic) eddy is marked with cyan (red) horizontal lines at the top of (a) and (g) and projected through all panels.

the smallest number among the following is chosen as k_{max} in this study: (i) the lowest frequency that shows corruption of the shear signal by vibrations, (ii) wavenumber of 150 cpm due to the spatial resolution of the shear probe, (iii) the cutoff frequency of the anti-aliasing filter, (iv) an estimate of the wavenumber that resolves 90% of the shear variance according to the Nasmyth spectrum as in Lueck (2013), and (v) the location of the spectral minimum determined with a low-order fit to the spectrum in log–log space.

b. Diffusivity

The diapycnal turbulent eddy diffusivity (K_ρ), and hereinafter referred to as diffusivity, can be estimated from the turbulent kinetic energy dissipation rate ε using the Osborn (1980) relation

$$K_\rho = \Gamma \frac{\varepsilon}{N^2}, \tag{5}$$

where Γ is the mixing efficiency, taken as a constant of 0.2 (Gregg et al. 2018).

c. Mixed layer depth, relative vorticity, potential vorticity, and geostrophic velocity

Here we define the mixed layer depth (MLD), as the depth at which the potential density changes by 0.03 kg m^{-3} from the value at 15 m (de Boyer Montegut et al. 2004). The vertical component of the relative vorticity (ζ) can be written as

$$\zeta = \frac{\partial v}{\partial x} - \frac{\partial u}{\partial y}, \tag{6}$$

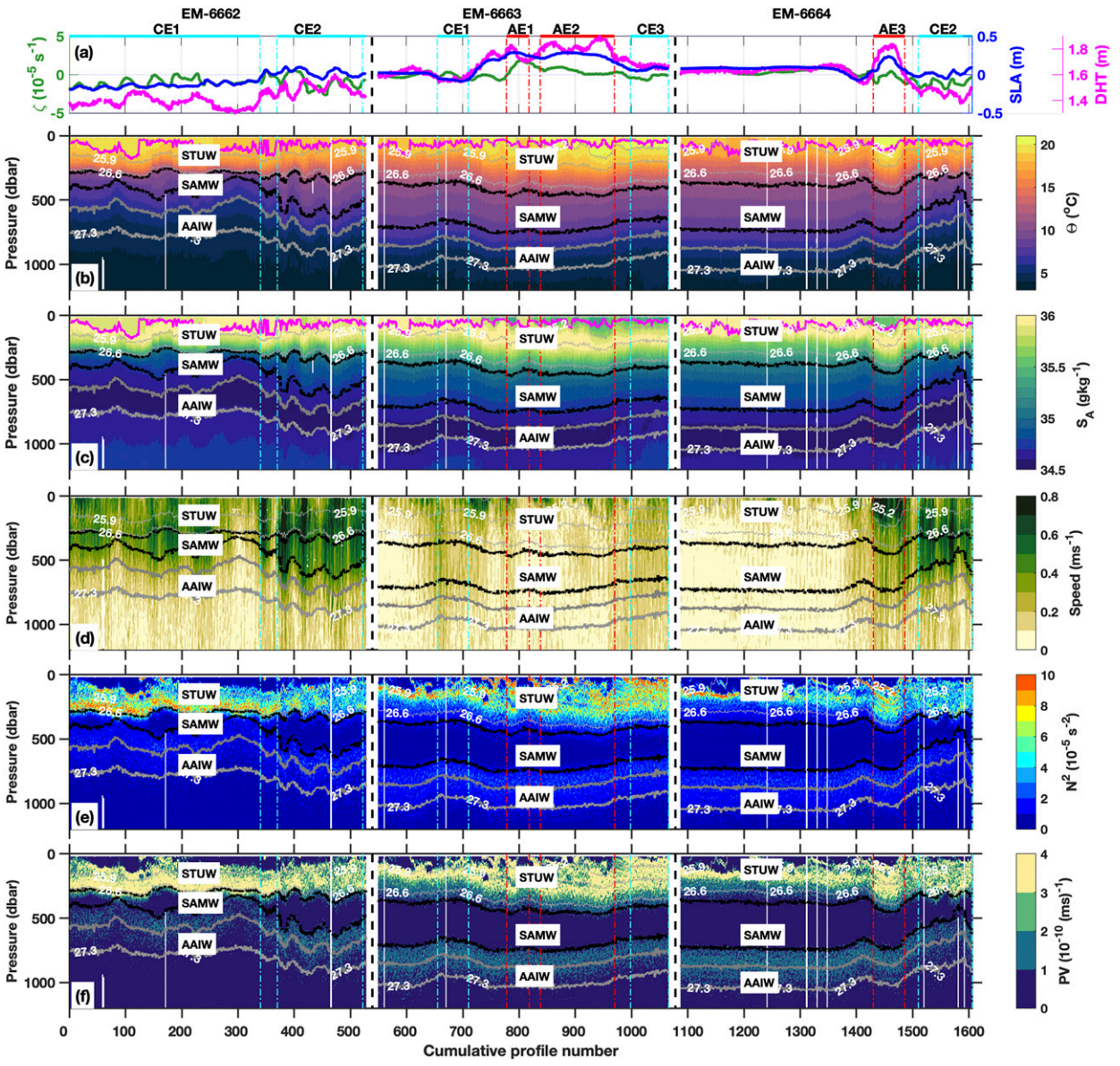

FIG. 4. As in Fig. 3, but along the float tracks. EM-6662 profiled two cyclonic eddies (CE1 and CE2). EM-6663 profiled two anticyclonic eddies (AE1 and AE2). EM-6664 profiled another anticyclone (AE3) and the same cyclonic eddy in EM-6662 (CE2). The evolution of the mixed layer depth along the float tracks is marked over temperature and salinity (magenta line). The x axis is cumulative profile number, which represents the evolution in time within each float's record.

where u (v) is the daily surface geostrophic eastward (northward) velocity component obtained from satellite altimetry. The ζ values are then subsampled at the time and location of each float profile to construct the along-trajectory variations. Similarly, the relative vorticity along the ship tracks were also estimated from satellite altimetry. Relative vorticity helps us to identify the mesoscale eddies in the float tracks where Southern Hemisphere anticyclonic (cyclonic) eddies have positive (negative) ζ values within their perimeter.

The potential vorticity (PV) can be written as $Q = [(f + \zeta)/\rho](\partial\rho/\partial z)$, where f is the planetary vorticity and ζ is the relative vorticity. In regions of weak currents, ζ is small relative to the planetary vorticity and thus the PV can be written as $Q = fN^2/g$, following Talley (2011), where g is the acceleration due to gravity (9.8 m s^{-2}). Since the LADCP velocities had large errors, we have calculated geostrophic velocities from the shipboard CTD data with a level of no motion of 1500 m. This level lies beneath the slow northward movement of the Antarctic Intermediate Water (not shown) and has previously been used as a reference level in the region (Stramma and Lutjeharms 1997; Menezes et al. 2014).

4. Observed water-mass structure and circulation

The surface layer in the southeast Indian Ocean south of 21°S along the Western Australian coast is dominated by warm

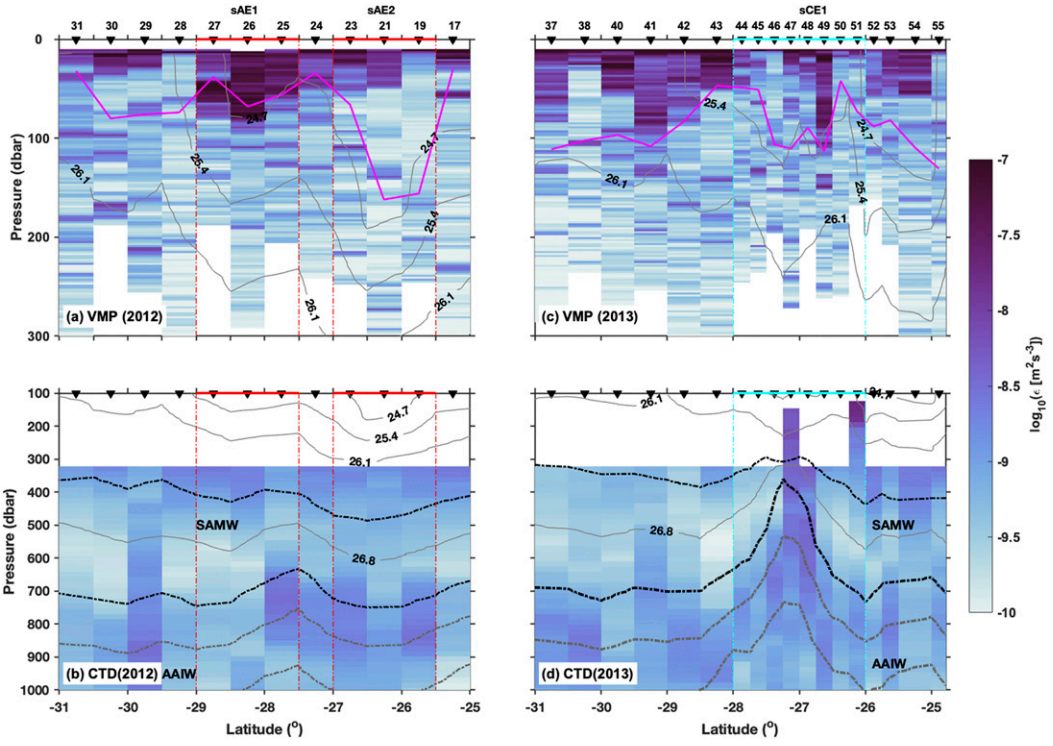

FIG. 5. Dissipation rate along 105°E ship tracks during 2012 from (a) VMP and (b) strain-only parameterization. (c),(d) As in (a) and (b), but from 2013. The gray contours are potential density at every 0.7 kg m^{-3}. The magenta lines in (a) and (c) are MLD during both years. The water masses and eddies are the same as in Fig. 3.

(>22°C), low salinity (<35.1 psu) tropical water with the temperature–salinity characteristics of LC water (Woo and Pattiaratchi 2008). Beneath the surface layer is the subtropical underwater (STUW) (Toole and Warren 1993) and South Indian Central Water (SICW) (Warren 1981), which are associated with subduction in the subtropics. The STUW can be identified as the shallow salinity maximum layer at around a potential density, σ_θ of 26.0 kg m^{-3}, whereas the SICW is the main part of the pycnocline just below STUW. The Subantarctic Mode Water (SAMW), which has a potential vorticity minimum, is found at the bottom of the SICW. The SAMW in the eastern Indian Ocean is stronger and thicker than that in the west and is called the Southeast Indian Subantarctic Mode Water (SEISAMW), with a characteristic temperature of 8°–9°C, salinity of 34.55 psu, and σ_θ of 26.8–26.9 kg m^{-3} (Thompson and Edwards 1981; Hanawa and Talley 2001). The salinity minimum at the base of the Central Water is the Antarctic Intermediate Water (AAIW), typically found at a depth of about 1000 m in the σ_θ range of 27.0–27.3 kg m^{-3} (Talley 2011).

a. Shipboard observations

The mesoscale eddies along the ship tracks can be identified from daily maps of SLA and relative vorticity. In 2012, the ship sampled two anticyclonic eddies along 105°E with VMP and CTD measurements (Figs. 3a–d). The anticyclonic eddy with center at station 26 (sAE1) is smaller than that at station 21 (sAE2). The dynamic height (DHT, 50/1500 dbar) along the track shows the location of each station with respect to the eddy center with sAE2 having higher values compared to sAE1. The sAE1 eddy also has weak signature in the SLA (0.2 m) compared to sAE2 (0.45 m). However, both have similar relative vorticity signatures (1×10^{-5} s^{-1}). The SLA plots show that sAE1 was a small eddy detaching from sAE2 during the sampling (not shown). Both eddies carried warm and fresh LC water in their center (Figs. 3b,c) above the salinity maximum of STUW. Higher geostrophic speed (>1 m s^{-1}) is observed at the edges of the eddies up to a depth of about 600 m (Fig. 3d). The isopycnals are affected up to a depth of about 2000 m especially for sAE2. The eddy sAE2 has a deeper mixed layer (160 m) than sAE1 (70 m). The different water masses along the track can be identified from the temperature and salinity data. The AAIW is observed between 800 and 1000 m as a salinity minimum between 27.1 and 27.3 kg m^{-3} (Fig. 3c). The anticyclones push down the AAIW to a slightly deeper depth. The SAMW can be identified as a potential vorticity minimum ($<1 \times 10^{-10}$ m^{-1} s^{-1}), above the AAIW between 26.7 and 26.9 kg m^{-3}, in a depth range of 300–700 m (Fig. 3f). The thickness of the AAIW layer does not change much in the anticyclonic eddies, whereas the SAMW layer shrinks considerably at the center of the cyclonic eddy. The buoyancy frequency is high at the base of the mixed layer and also below the lower layer of SAMW (Fig. 3e).

In 2013, VMP and CTD measurements were repeated along the transect (Figs. 3g–l) and EM-APEX floats were deployed (Fig. 1c). The ship sampled a cyclonic eddy that had a significant signature in SLA and relative vorticity (Fig. 3g). DHT also decreases toward

TABLE 2. Mean and one standard deviation of dissipation rate ($m^2 s^{-3}$) and diffusivity ($m^2 s^{-1}$) at different depth ranges from VMP for 2012 and 2013 in both cyclonic (CE) and anticyclonic (AE) eddies.

Depth	Dissipation rate		Diffusivity	
	2012	2013	2012	2013
ML	$(2.25 \pm 2.2) \times 10^{-8}$	$(4.4 \pm 9) \times 10^{-8}$	$(8.9 \pm 7.7) \times 10^{-4}$	$(1.6 \pm 3) \times 10^{-3}$
ML AE	$(2.84 \pm 2.5) \times 10^{-8}$	—	$1.0 \times 10^{-3} \pm 8.8 \times 10^{-4}$	—
ML CE	—	$(1.54 \pm 1.4) \times 10^{-8}$	—	$(2.6 \pm 5.1) \times 10^{-3}$
0–300-m AE	$(5.91 \pm 0.17) \times 10^{-9}$	—	$1.82 \times 10^{-4} \pm 0.0018$	—
0–300-m CE	—	$(4.5 \pm 0.34) \times 10^{-9}$	—	$5.62 \times 10^{-4} \pm 0.012$
0–300-m total	$(4.9 \pm 0.16) \times 10^{-9}$	$(1.14 \pm 0.22) \times 10^{-8}$	$1.54 \times 10^{-4} \pm 0.0015$	$4.03 \times 10^{-4} \pm 0.0065$

the center of the eddy from the edges. The isopycnals were affected below 400 m with little impact near the surface. At the center, the cyclonic eddy carried warm surface water of about 20°C and slightly less saline water than STUW. From stations 52–55, the surface waters were warmer and fresher compared to the center of the cyclonic eddy. The sea level anomaly plots show the presence of an anticyclonic eddy at this location that was not fully developed (Fig. 1c). It had no signature in relative vorticity (Fig. 3g) and no deepening of isopycnals associated with the warm and freshwater at the surface (Figs. 3h,i). The AAIW was observed at the same depth as in 2012 except within the cyclonic eddy, where SAMW was uplifted to a depth of about 400 m and AAIW to a depth of about 600 m. The thickness of the SAMW layer was significantly reduced at the center of the cyclonic eddy.

b. *EM-APEX floats*

The floats were strongly influenced by the eddy field at different times along their track. In Fig. 4, the float profiles are presented as time series with a vertical line separating each float. The horizontal axis is cumulative profile number, which represents both distance along the trajectory and time, but allows a uniform spacing between profiles. The SLA and relative vorticity along the float tracks identify the eddies comparatively well irrespective of their coarse resolution. They mostly follow the pattern of DHT especially in regions of eddies. EM-6662 was deployed in the cyclonic eddy centered at station 47 (Fig. 1c). This float looped around the eddy and moved south with the eddy. After a while, EM-6662 came out of that cyclonic eddy (CE1) and started to profile around another cyclonic eddy (CE2) until its battery died. The isopycnals in CE2 were more strongly uplifted at depths below 300 m suggesting that it is a subsurface-intensified eddy. The SAMW and AAIW were uplifted to shallow depths as in the shipboard data. CE2 had stronger rotational velocities, compared to CE1, which extended to the depth of AAIW (Fig. 4d).

The other two deep floats (EM-6663 and EM-6664) were deployed south of the eddy CE1 (Fig. 1c). EM-6663 continuously profiled toward the north through the western flank of CE1 and the southern edge of two warm core eddies (AE1 and AE2). It then profiled around the western edge of another cyclonic eddy, CE3. The presence of AE1 and AE2 is more evident from DHT, SLA, and relative vorticity with little signature on the depth of isopycnals. In contrast, CE1 and CE3 have less surface signature in DHT, SLA, and relative vorticity with shoaling of isopycnals at depths below 400 m.

EM-6664 profiled north for a while without interacting with any eddy and this is evident from the SLA and relative vorticity along its track. The DHT also varied very little along this part of the track. It then profiled the southern edge of a big anticyclonic eddy (AE3) with a strong signature in DHT and SLA and weak signature in relative vorticity; it was then caught up in the same cyclonic eddy (CE2) that trapped EM-6662. The eddy carries fresh and warm LC water in its center with a deep mixed layer. Deepening of isopycnals was evident to below 1200 m in the anticyclonic eddy.

TABLE 3. Mean and one standard deviation of dissipation rate ($m^2 s^{-3}$) and diffusivity ($m^2 s^{-1}$) at different depth ranges from strain-only parameterization in both cyclonic (CE) and anticyclonic (AE) eddies.

Depth	Dissipation rate		Diffusivity	
	2012	2013	2012	2013
400–1000 AE	$(8.1 \pm 3) \times 10^{-10}$	—	$(1.2 \pm 0.4) \times 10^{-5}$	—
400–1000 CE	—	$(9.9 \pm 3.1) \times 10^{-10}$	—	$(1.7 \pm 0.5) \times 10^{-5}$
400–1000 all	$(8.3 \pm 3) \times 10^{-10}$	$(9 \pm 2.6) \times 10^{-10}$	$(1.3 \pm 0.4) \times 10^{-5}$	$(1.5 \pm 0.36) \times 10^{-5}$
1000–bottom CE	—	$(4.2 \pm 1.6) \times 10^{-10}$	—	$(4.7 \pm 1.3) \times 10^{-5}$
1000–bottom all	—	$(3.2 \pm 1.3) \times 10^{-10}$	—	$(3.5 \pm 9.8) \times 10^{-5}$
SAMW AE	$(6.3 \pm 1.7) \times 10^{-10}$	—	$(1.0 \pm 0.3) \times 10^{-5}$	—
SAMW CE	—	$(1.2 \pm 0.34) \times 10^{-9}$	—	$(9.8 \pm 1.4) \times 10^{-6}$
SAMW all	$(5.8 \pm 1.6) \times 10^{-10}$	$(8.2 \pm 2.6) \times 10^{-10}$	$(1.1 \pm 0.3) \times 10^{-5}$	$(9.7 \pm 1.4) \times 10^{-6}$
AAIW AE	$(9.6 \pm 3.5) \times 10^{-10}$	—	$(1.3 \pm 0.41) \times 10^{-5}$	—
AAIW CE	—	$(1.4 \pm 0.21) \times 10^{-9}$	—	$(2.2 \pm 0.33) \times 10^{-5}$
AAIW all	$(1.1 \pm 0.3) \times 10^{-9}$	$(1.2 \pm 0.18) \times 10^{-9}$	$(1.5 \pm 0.36) \times 10^{-5}$	$(1.9 \pm 0.27) \times 10^{-5}$

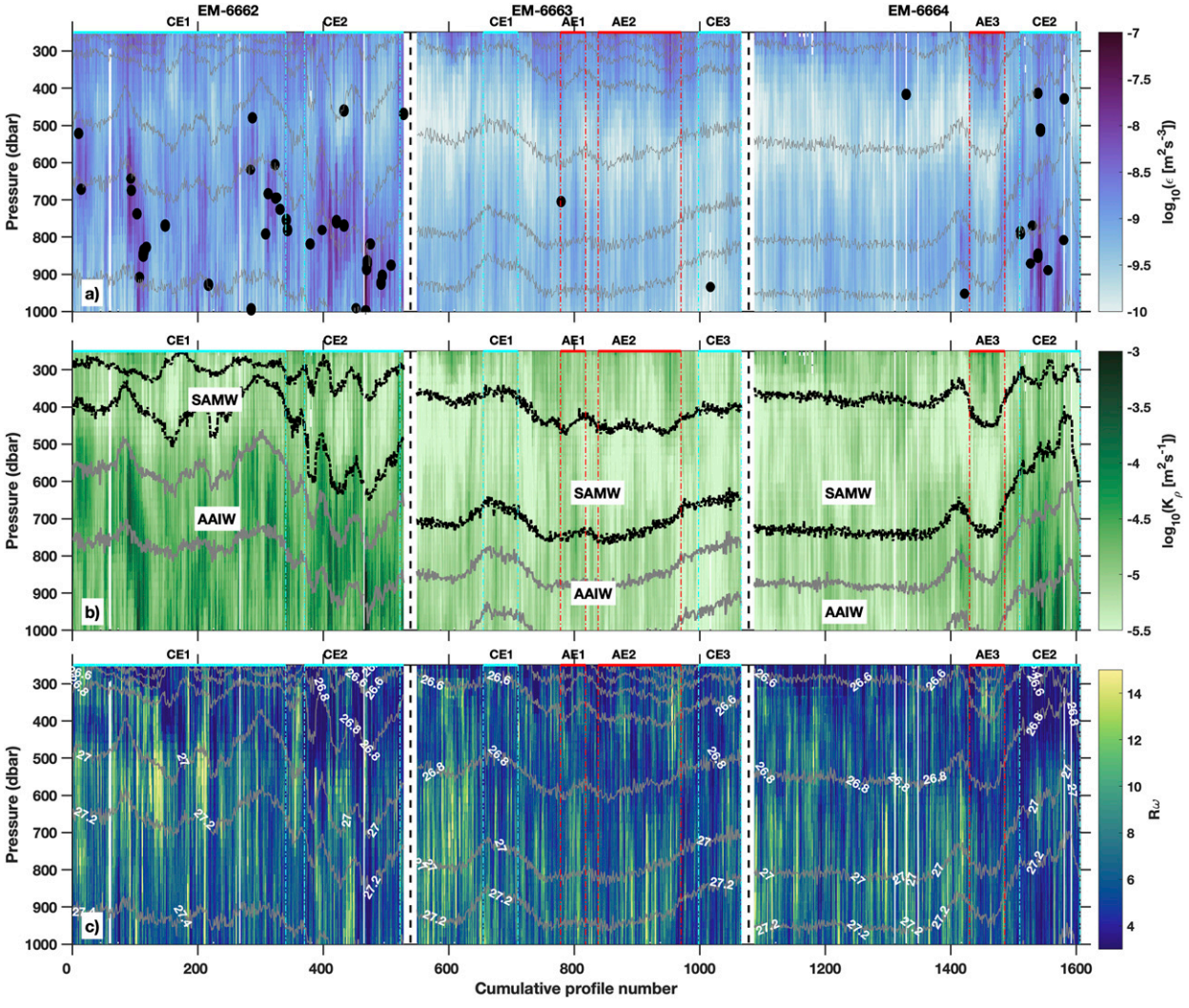

FIG. 6. The evolution of (a) dissipation rate, (b) diffusivity, and (c) shear–strain variance ratio along the float tracks. The eddies are as described in Fig. 4. The vertical extent of SAMW (26.7–26.9 kg m^{-3}) and AAIW (27.1–27.3 kg m^{-3}) is marked in (b). The gray contours are potential density as labeled in (c). The black patches in (a) mark the regions with Ri < 0.25.

The floats provide a finer picture of the different water masses in this region than the ship based CTD data. Warm, salty STUW lies at the surface in profiles south of around 26°S. North of 25°S, the STUW is found beneath the warmer fresher waters of the Indonesian–Australian basin, which is supplied by the Indonesian Throughflow (Figs. 4b,c, EM-6663). In anticyclonic eddies, the STUW is capped by a warm fresh layer that is possibly LC water that was trapped during the formation of the eddy close to the Australian coast (Morrow et al. 2003; Mao et al. 2018). The thickness of the SAMW layer varies considerably along the tracks of EM-6662 and EM-6664, becoming very thin when they encountered cyclonic eddies (Figs. 4e,f). The AAIW layer also was uplifted to shallower depths by the cyclonic eddies. The impact of eddies on the depths of different water masses is clearly visible from the track of EM-6664, which recorded conditions in the presence of a cyclonic eddy, an anticyclonic eddy, and no eddies (Fig. 4f).

5. Mixing variability in the upper 1000 m

a. Microstructure

The microstructure measurements from 2012 and 2013 show that dissipation rate is highly variable in the upper 300 m (Figs. 5a,c). In both 2012 and 2013, we observe elevated dissipation rate within the mixed layer as expected. Below the mixed layer, the dissipation rate falls to background levels with a change of about three–four orders of magnitude with depth. The mean and standard deviation of dissipation rate and diffusivity at different depth ranges and in different eddies is given in Table 2. The surface diffusivity in sAE1 is slightly higher (9.8×10^{-4} m^2 s^{-1}) than that in sAE2 (3.8×10^{-4} m^2 s^{-1}). The elevated dissipation rate at the center of sAE1 extends to the base of the mixed layer, whereas in sAE2, the elevated dissipation rate does not extend that deep (Fig. 5a). The mean dissipation rate in the cyclonic eddy in

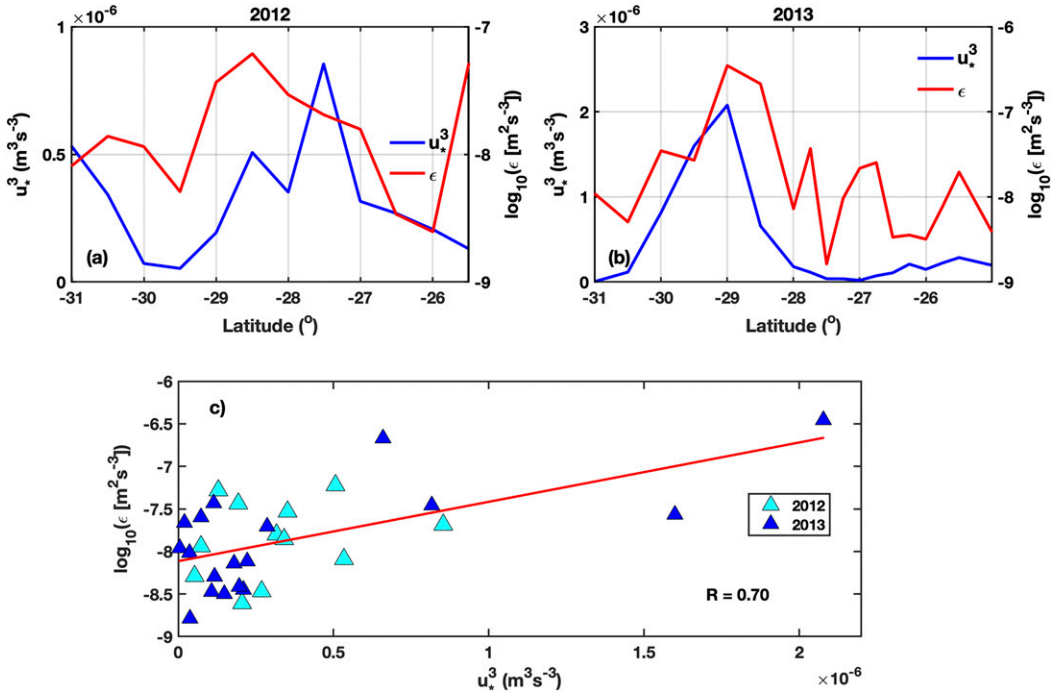

FIG. 7. Mean dissipation rate (red line) in the mixed layer and estimates of cube of wind stress friction velocity ($u*$) from wind measured from the ship (blue line) during (a) 2012 and (b) 2013 along the transects. (c) Scatterplot of cube of $u*$ and mean dissipation rate from VMP in 2012 (cyan triangle) and 2013 (blue triangle). The red line in (c) is the best fit line estimated from all data from both years, with correlation coefficient R.

2013 is slightly weaker than that of the anticyclonic eddies of 2012 (Table 2).

b. *Strain-only parameterization*

The estimates of dissipation rate from the shipboard CTD data between 400 and 1000 m also show spatial variability over the transects and with depth (Figs. 5b,d). The diffusivity estimates have a similar pattern. In 2012, the mean dissipation rate from the strain-only method is $8.3 \times 10^{-10}\,m^2\,s^{-3}$ with a standard deviation of $3 \times 10^{-10}\,m^2\,s^{-3}$. The diffusivity is elevated in the anticyclonic eddies, sAE1 and sAE2 ($10 \times 10^{-5}\,m^2\,s^{-1}$) and is slightly higher than the mean in 2012. The mean dissipation rate in 2013 is $9 \times 10^{-10}\,m^2\,s^{-3}$ with a standard deviation of $3 \times 10^{-10}\,m^2\,s^{-3}$. The dissipation rate and diffusivity are elevated in the cyclonic eddy in 2013 above 1000 m (Table 3). In the cyclonic eddy, the diffusivity in AAIW layer is 2 times larger than that in the SAMW layer. Although, the pattern of dissipation rate between VMP and strain-only method at the intersecting depth range is quite different, there are some profiles that have qualitative similarity between VMP measurements and strain-only estimates. For instance, several profiles at the southern end of the transect in 2013 (Figs. 5c,d) show lower dissipation rate between 200 and 600 m. A more detailed discussion on this is provided in section 7a.

c. *Shear–strain parameterization*

The dissipation rate and diffusivity estimates from the float data using the shear–strain parameterization also show strong variability between 200 and 1000 m (Fig. 6). Regions of enhanced dissipation rate are often associated with Ri < 0.25 (Fig. 6a), where Ri is the Richardson number [$\mathrm{Ri} = N^2/(\partial u/\partial z)^2$, and $\partial u/\partial z$ is the vertical shear of the horizontal speed. Here, both the velocity and density gradients with 3 m resolution in the vertical are smoothed over 24 m to avoid the spectral roll-off region identified in the shear and strain spectra], indicating that in these regions the shear can overcome stratification and overturning can occur. The mean dissipation rate from the floats is $(1.1 \pm 1.2) \times 10^{-9}\,m^2\,s^{-3}$, which is slightly larger than the background levels observed in mid- and low latitudes of the global ocean (St. Laurent et al. 2012). The floats have a mean diffusivity of $1.7 \times 10^{-5}\,m^2\,s^{-1}$ with a standard deviation of $2.9 \times 10^{-5}\,m^2\,s^{-1}$. Mesoscale eddies play an important role in the spatial distribution of diffusivity. Comparatively high diffusivity is observed in cyclonic eddies below the surface (CE1 and CE2) and in anticyclonic eddies near the surface (AE1, AE2, and AE3) (Fig. 6b, Table 3). For example, EM-6662, which was caught up in two cyclonic eddies, recorded elevated diffusivity below 250 m ($5.4 \times 10^{-5}\,m^2\,s^{-1}$ for profiles from 85 to 120). For EM-6663, which encountered virtually no eddies, diffusivity is mostly on background levels [$O(10^{-6})\ m^2\ s^{-1}$]. EM-6664 had weak diffusivities during the earlier, eddy-free part of its track ($11 \times 10^{-6}\,m^2\,s^{-1}$), followed by elevated diffusivity in the anticyclonic eddy in the upper 350 m and in the cyclonic eddy below 250 m (Table 3). This is in agreement with the elevated diffusivity observed in both cyclonic and anticyclonic eddies from

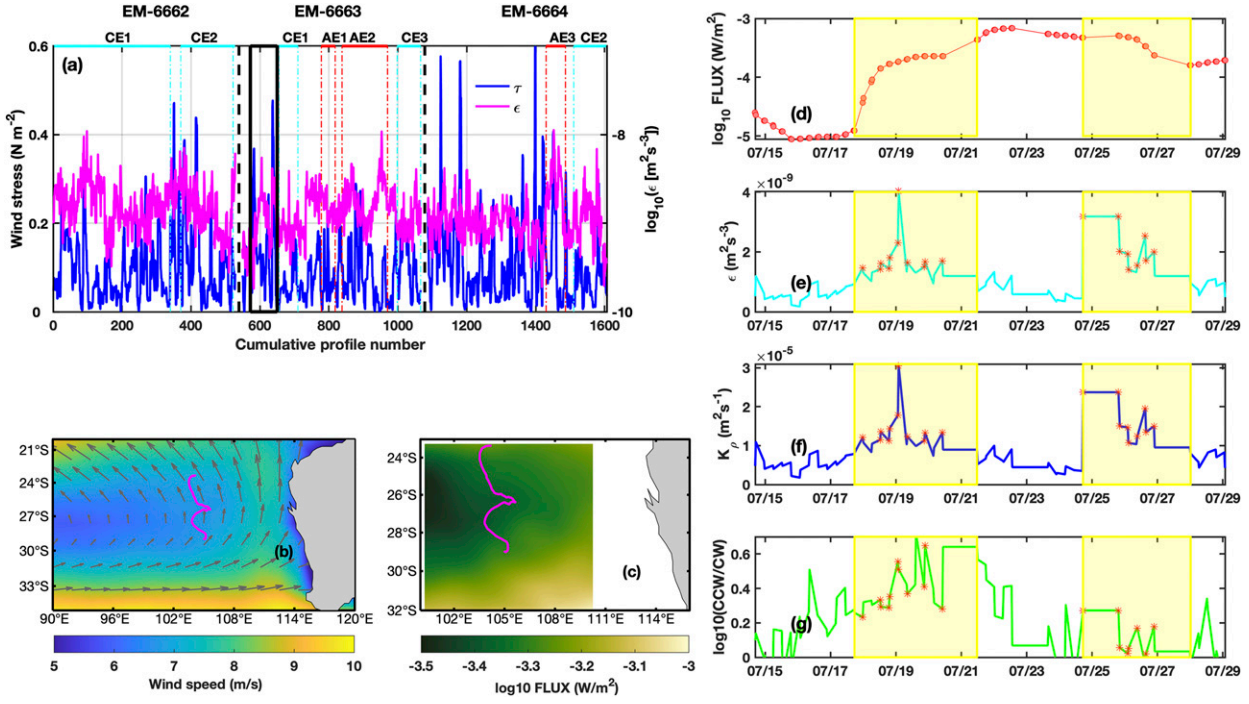

FIG. 8. (a) Mean dissipation rate (magenta line) in the depth range 250–350 m along the float tracks and NCEP wind stress (blue) at the time and location of the floats. The black thin dashed line separates the floats. The region in the thick black box represents the profiles that are examined in the right panels. (b) Mean spatial map of wind speed (color shading) over the region during the profiling of float EM-6663. The gray arrows show the mean direction of wind and the pink line shows the track of float EM-6663. (c) Mean spatial map of wind energy flux into near-inertial motions from May to October 2013 with the float track in pink. (d) Energy flux averaged over 15–20 days prior to each float mixing estimate. Depth-averaged (e) dissipation rate, (f) diffusivity, and (g) polarization ratio in the upper 400 m over a period of 15 days along the track of the float EM-6663, within the black box in (a). The red stars in (d)–(g) are values above the mean, highlighted with yellow shaded boxes.

the VMP and shipboard data. Although the distribution of R_ω along the float tracks is rather noisy, some patterns are distinguishable. For instance, the elevated mixing in regions of anticyclonic eddies near the surface ($\sim$ 200 m) is often associated with higher values of R_ω suggesting the presence of near-inertial waves (e.g., AE3 in float EM-6664 of Fig. 6c).

6. Mixing distribution and influencing factors

Here we investigate the factors that influence the observed mixing variability from floats, shipboard CTD and VMP. The potential candidates are wind stress at the surface, mesoscale eddies, and bottom topography, with internal wave propagation upward or downward depending on the source, and reflections from the boundaries. There are examples of enhanced dissipation throughout the water column, as shown in Fig. 5, some near the sea surface, most likely to be generated by wind forcing, and some at depth.

a. Wind stress

The wind blowing over the ocean surface generates near-inertial motions in the mixed layer. These motions further excite internal waves at the base of the mixed layer that propagate downward into the ocean interior (e.g., Alford 2003). These waves are expected to provide a major portion of the energy needed to support the global overturning circulation (Munk and Wunsch 1998). From the float data, we have identified many vertically propagating near-inertial waves. In this section, we investigate the impact of wind forcing on turbulent mixing estimates.

The ocean mixed layer is primarily forced by solar heating, turbulent fluxes, and wind stress. The impact of shear instabilities at the base of the mixed layer due to internal wave breaking contributes less to the mixed layer turbulence where air–sea interaction and convective instabilities dominate (Greenan et al. 2001; Garrett 2003). Some studies have shown that the dissipation of turbulent kinetic energy [$\varepsilon(z)$] scales with depth z as $u_*^3/\kappa z$ where u_* is the wind stress friction velocity and κ is the von Kármán constant (e.g., Dillon and Caldwell 1980; Dillon et al. 1981; Oakey and Elliott 1982; Greenan et al. 2001). Here, $u_* = \sqrt{(\tau/\rho)}$ where τ is the wind stress calculated from shipboard measurements of wind speed with an air density of 1.22 kg m^{-3} and coefficient of friction, Cd = 1.3 $\times$ 10^3. In these studies, a significant difference in dissipation rate was found in high and low wind conditions. We thus looked at u_*^3 and dissipation rate from VMP in the mixed layer in 2012 and 2013. VMP measurements show elevated dissipation rate in the mixed layer that varies along the track (Figs. 7a,b). In 2013, the u_*^3 peaks around 29°S and drops rapidly toward the north with a similar pattern in dissipation

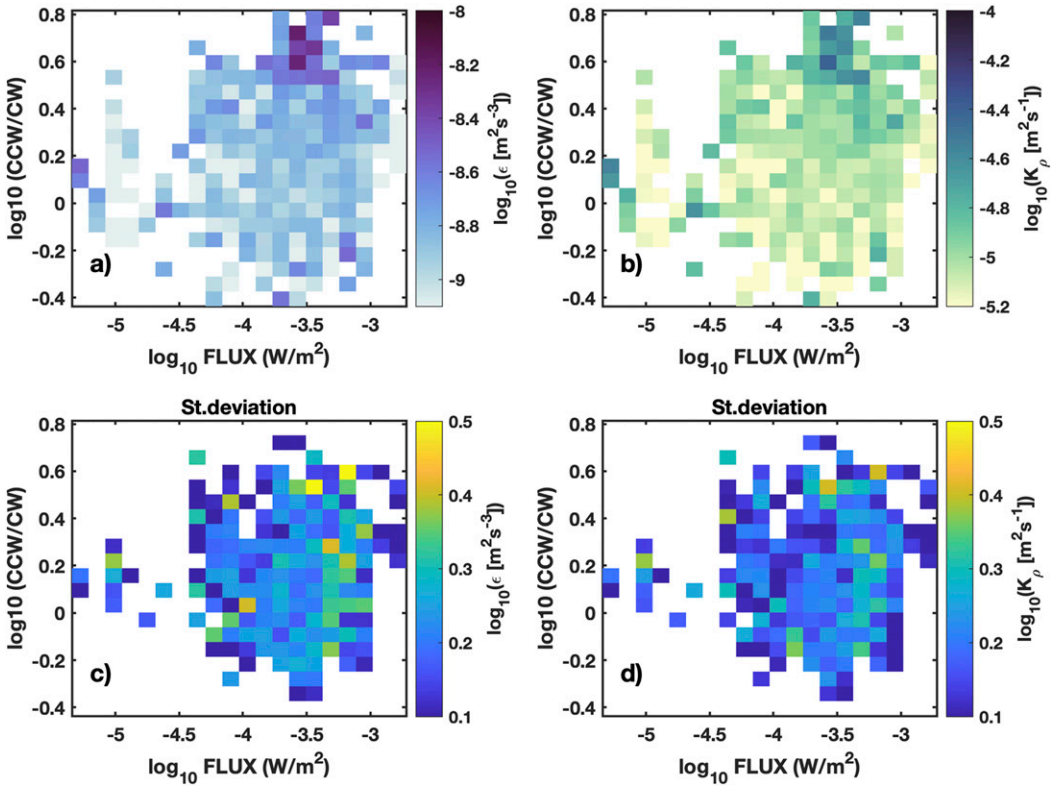

FIG. 9. Mean (a) dissipation rate and (b) diffusivity below the mixed layer between 250 and 350 m as a function of wind energy flux into near-inertial motions and polarization ratio. (c),(d) The corresponding one standard deviations.

rate (Fig. 7b). In 2012, the pattern is less evident (Fig. 7a). Nevertheless, there is a strong correlation (0.71) between u_*^3 and dissipation rate in the mixed layer when data from both years are combined (Fig. 7c). This suggests that wind forcing could be a strong contributor to mixed layer turbulence in this region. A detailed investigation of the dominant mechanisms of mixed layer turbulence in this region will be the focus of a future study. Here, we concentrate on mixing below the mixed layer.

The floats provide mixing estimates only below the mixed layer. Thus, we examine the distribution of dissipation rate in the upper 250–350 m and the wind stress at each float location to look for evidence of wind-driven mixing (Fig. 8a). The wind in this region has an equatorward component throughout the year (Godfrey and Ridgway 1985; Fig. 8b) that is stronger during austral summer (McCreary et al. 1986). During the four-month lifetime of the floats, they encountered both weak and a few strong ($>0.5\,\mathrm{N\,m^2}$) wind events. More than 250 float profiles were collected from locations of strong wind events where the wind stress is larger than two standard deviations from the mean along each float track. Elevated dissipation rate and diffusivity is often observed below the mixed layer following strong wind events in regions of noneddy activity (e.g., profiles between 590 and 650), as well as in anticyclonic eddies (e.g., profiles between 1450 and 1460) and cyclonic eddies (e.g., profiles between 380 and 400) as in Fig. 8a.

To explore the relationship between mixing and wind-generated near-inertial waves, a slab model developed by Pollard and Millard (1970) without mesoscale currents is applied to the reanalysis wind time series to estimate the near-inertial mixed layer velocity components. The wind energy flux into near-inertial motions is then estimated as $\Pi = \tau U_{\mathrm{in}}$, where τ is the wind stress and U_{in} is the near-inertial velocity (e.g., Silverthorne and Toole 2009). A detailed derivation and discussion of the model can be found in the works of D'Asaro (1985), Silverthorne and Toole (2009), Alford (2003), and Alford et al. (2012). We run the model with a constant mixed layer depth of 70 m, which is the mean value obtained from the float data and a Rayleigh damping parameter of 1/(2 days) (Whalen et al. 2018). Following Whalen et al. (2018), we then averaged the energy flux 15–20 days before each mixing profile from the floats by considering the time span for a near-inertial wave of vertical velocity $\sim 20\,\mathrm{m\,day^{-1}}$ to reach 400 m. The energy flux is comparatively low in the southeast Indian Ocean (Fig. 8c) with higher values toward the south.

In Figs. 8d–g, we further zoom into the float record in a noneddy activity region of float EM-6663, from profiles 572–650. We observe elevated energy flux from winds corresponding to higher than mean values of dissipation rate and diffusivity estimates in the float track during this 15-day period (Figs. 8d,e, yellow shading). The energy flux is the average of 15–20 days prior to each mixing estimate. Higher polarization ratio is also observed indicating downward propagation of near-inertial waves (Fig. 8g), and there are strong near-inertial wave beams with amplitudes larger than $20\,\mathrm{cm\,s^{-1}}$ observed at

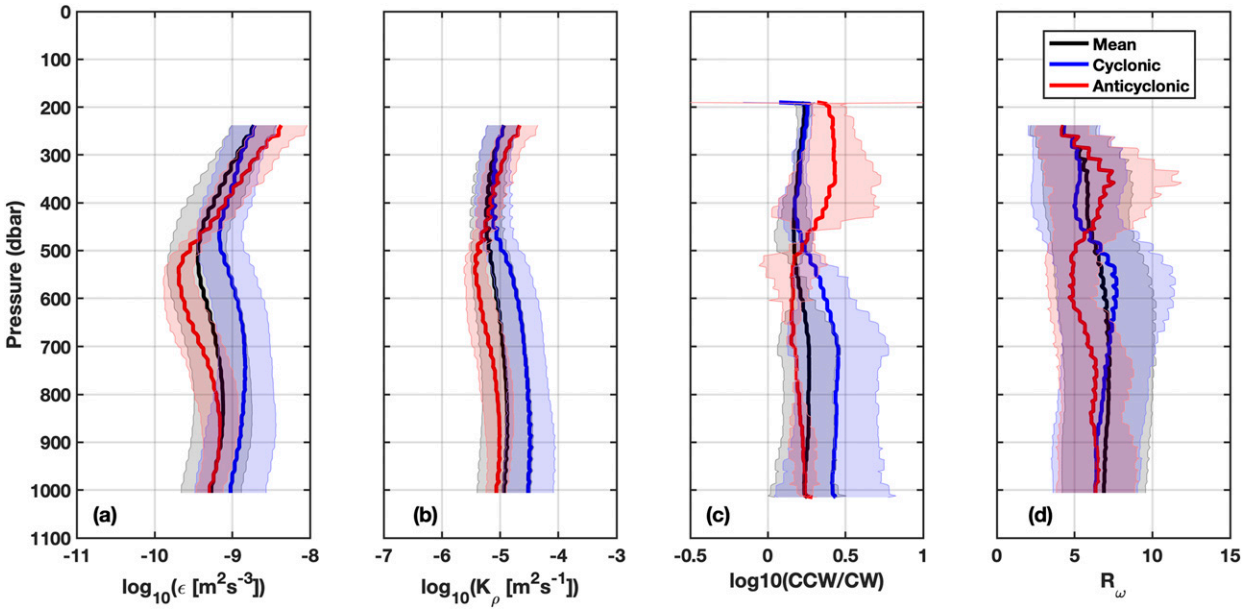

FIG. 10. Vertical distribution of (a) dissipation rate, (b) diffusivity, (c) polarization ratio, and (d) shear–strain variance ratio in regions of cyclonic (blue) and anticyclonic (red) eddies along with the mean (black) of all profiles. The shading in all panels is one standard deviation.

the same (Cyriac et al. 2021, manuscript submitted to *J. Phys. Oceanogr.*). This suggests that the higher values of polarization ratio are characterized by downward-propagating near-inertial waves, consistent with wind forcing being the dominant source of enhanced dissipation rate in the upper water column.

To further explore the relationship between mixing and wind-generated near-inertial waves, we looked at the distribution of mixing estimates with near-inertial energy flux and polarization ratio in the upper 250–350 m (Fig. 9). Wind stress fluctuations add energy into the mixed layer near the inertial frequency, and generate internal waves that dissipate as they propagate down into the ocean interior (Alford et al. 2012). The higher values of dissipation rate and diffusivity are associated with increased wind energy flux and dominant CCW propagation (Figs. 9a,b). This is in agreement with the process of wind-generated downward-propagating internal waves, reinforcing the idea of surface wave generation.

b. Mesoscale eddies

The propagation of near-inertial waves generated at the ocean surface can be influenced by mesoscale eddies. Here we investigate the diffusivity estimates associated with both cyclonic and anticyclonic eddies in the float data. The floats returned a total of 1566 profiles among which 231 profiles are associated with anticyclonic eddies and 721 profiles with cyclonic eddies.

In the upper 400 m, higher dissipation rate is observed within anticyclonic eddies (Fig. 10a, Table 3). The dissipation rate in cyclonic eddies at this depth range is lower than for anticyclonic eddies and is close to the mean value. For instance, the mean dissipation rate in the upper layer of anticyclonic eddy (AE3) in float EM-6664 is $2.5 \times 10^{-9}\,\mathrm{m^2\,s^{-3}}$, which is 2 times larger than that in the cyclonic eddy CE2 ($1.2 \times 10^{-9}\,\mathrm{m^2\,s^{-3}}$) and ~3 times larger than the overall mean dissipation rate in the upper layer of float EM-6664 ($8 \times 10^{-10}\,\mathrm{m^2\,s^{-3}}$). It is also 2 times larger than the overall mean dissipation rate from all three floats ($1.1 \times 10^{-9}\,\mathrm{m^2\,s^{-3}}$). We see a similar distribution for the diffusivity in the upper 400 m (Fig. 10b). The polarization ratio in the anticyclonic eddies in the upper 400 m (Fig. 10c) shows that downward-propagating waves dominate at this depth range, suggesting that the elevated dissipation rate in the upper 400 m of the anticyclonic eddies is associated with downward-propagating waves. The shear-to-strain variance ratio is also enhanced in the upper 400 m of the warm core eddy (Fig. 10d) suggesting that the elevated mixing in the anticyclonic eddies near the surface is associated with near-inertial waves.

Both observational (e.g., Sheen et al. 2015; Whalen et al. 2018) and modeling (e.g., Balmforth and Young 1999) studies show elevated mixing in regions of anticyclonic vorticity near the surface. In theory, anticyclonic vorticity can reduce the propagating frequency of the near-inertial internal waves and thereby trap them, leading to wave breaking and enhanced dissipation rate (Kunze 1985). The elevated mixing observed in the anticyclonic eddies in this study is consistent with the coherent features in velocity profiles in AE3 with an upward phase propagation corresponding to a downward energy propagation near the surface (Figs. 11a–c). This reinforces the idea of wave trapping by the relative vorticity of the anticyclonic eddy. We observe elevated diffusivity in anticyclonic eddies [$O(10^{-4})\,\mathrm{m^2\,s^{-1}}$] in the upper 300 m from VMP measurements as well (Table 1).

In a cyclonic eddy, the waves generated at the surface can freely propagate out of the eddy, but they cannot penetrate

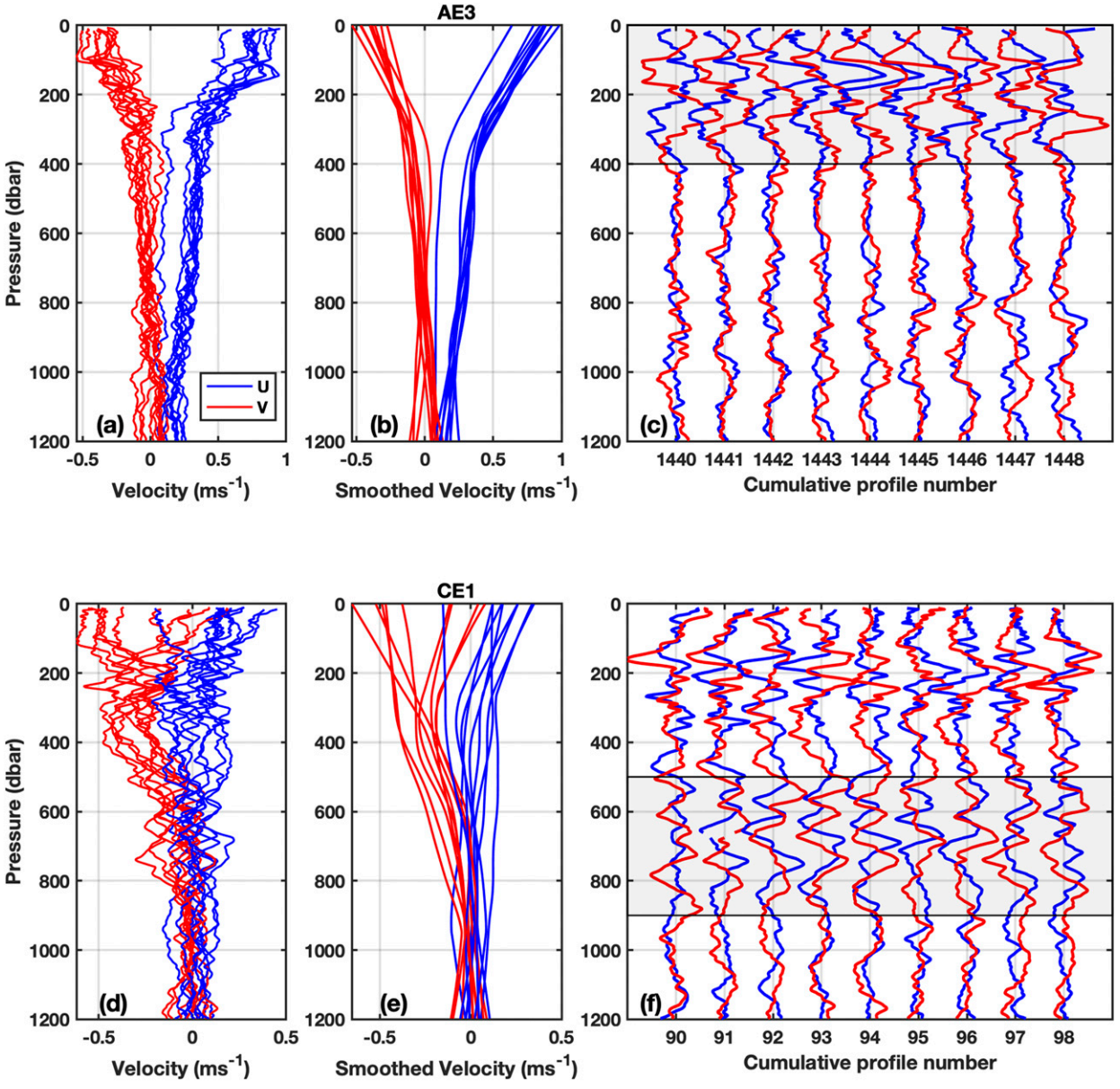

FIG. 11. (a) Zonal (blue) and meridional (red) components of velocity profiles of EM-6664 from cumulative profiles 1440–1448 in the anticyclonic eddy AE3. (b) Corresponding smoothed velocities from a vertical moving average window of 500 m. (c) Velocity anomaly obtained by subtracting smoothed velocity profiles from the measured velocity profiles. The gray shading identifies the coherent feature approximately between surface and 400 m. (d)–(f) As in (a)–(c), but for the cyclonic eddy CE1 in EM-6662. The gray shading between 500 and 900 m identifies another coherent feature.

into the core of a cyclonic eddy from outside (Kunze 1985). One exception though is outside the high velocity region of a cyclonic eddy where the change in sign of vorticity can result in wave trapping (Sanford 1984; Kunze 1985). From the float data, dissipation rate in cyclonic eddies is highest below 500 m compared to the upper water column (Fig. 10a). It is higher than that observed in anticyclonic eddies (2.5×10^{-9} m^2 s^{-3}) and also higher than the mean from all profiles at this depth range. There is a similar distribution for diffusivity (Fig. 10b). The polarization ratio is higher below 500 m in the cyclonic eddies compared to the upper water column (Fig. 10c). Coherent features in velocity profiles with upward phase propagation (downward energy propagation) are also observed in the location of elevated dissipation rate in the cyclonic eddies (Figs. 11d,f). This suggests that the higher dissipation rate in the cyclonic eddies below 500 m is associated with downward-propagating waves. This result is in contrast to Richardson et al. (1979) where they observed upward-propagating internal waves in a cyclonic eddy. The corresponding shear-to-strain variance ratio is low below 500 m in

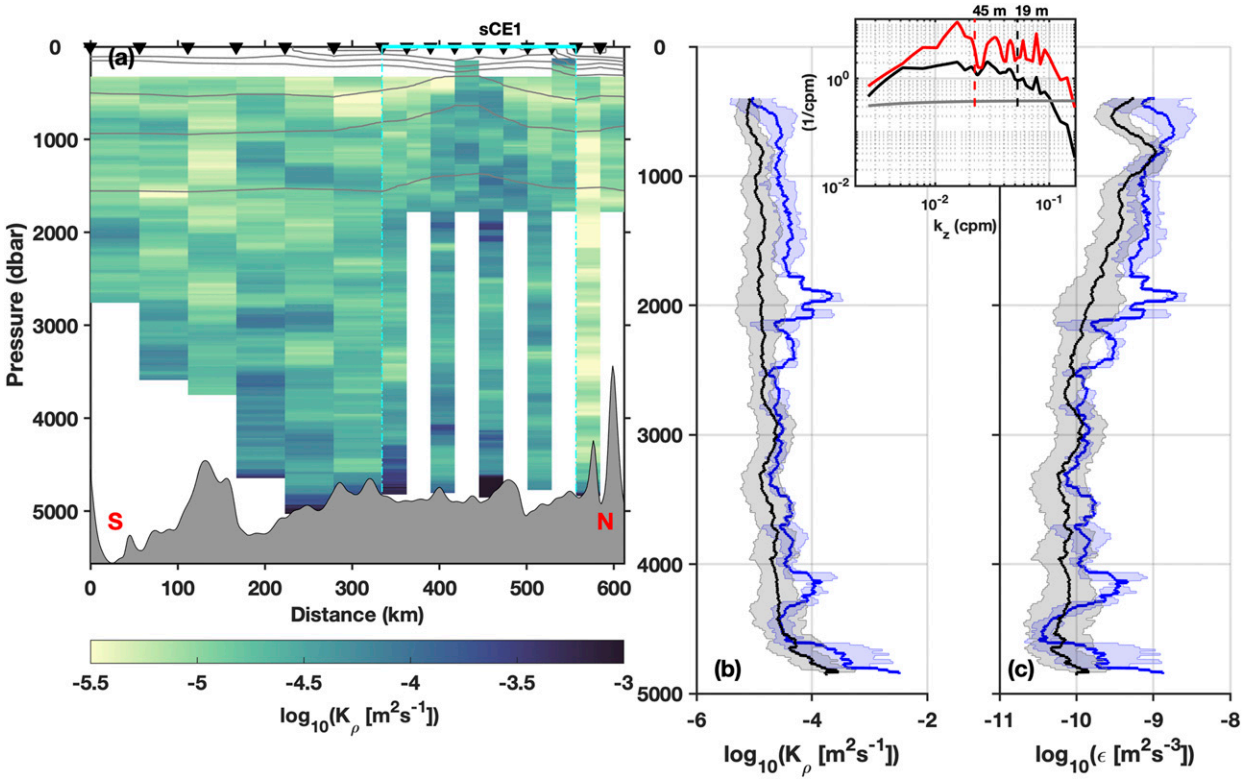

FIG. 12. (a) Estimates of diffusivity along the 105°E transect in 2013 using strain-only method. The x axis is the distance along the transect from the southernmost station (31°S). The gray lines are the isopycnals at every 0.4 kg m $^{-3}$. The cyclonic eddy is also marked. The vertical profile of mean (b) diffusivity and (c) dissipation rate for the transect with one standard deviation shading in the eddy (blue) and noneddy (black) regions. The inset plot shows the mean strain spectrum for the profile (black) having high bottom diffusivity at 450 km and the strain spectrum for the bottommost 500 m (red) where the mixing is high. The gray line is the GM spectrum, and the vertical dashed colored lines show the corresponding high wavenumber limit for each spectrum as indicated by the red/black color.

the cyclonic eddies (Fig. 10d). This suggests that the elevated dissipation rate in the cyclonic eddies below 500 m could be due to waves with frequencies outside the near-inertial band.

Since the eddy has cyclonic vorticity, we rule out the theory of wave trapping driven by anticyclonic relative vorticity (Kunze 1985). Another possibility is the concept of wave capturing where the horizontal strain $[(U_x - V_y)^2 + (U_x + V_y)^2]$ of the mesoscale field locally dominates relative vorticity (Bühler and McIntyre 2005; Polzin 2008). In the case of wave capture, strain exceeds relative vorticity, and therefore the vertical and horizontal wavenumbers of the internal waves will grow in magnitude and dissipate eventually (Bühler and McIntyre 2005; Polzin 2008). Captured waves tend to have a frequency higher than Coriolis and higher vertical wavenumber (Polzin 2008). Using altimetry data, we estimated the relative vorticity and horizontal strain along the float tracks and found mean values of 0.10f and 0.12f, respectively, corresponding to the feature in Fig. 11f. These estimates suggest that the effect of eddy strain field in capturing waves and potentially facilitating a mesoscale-to-wave energy transfer may have a larger effect on the enhanced turbulence rates here than the wave trapping and dissipating mechanisms. The effect of wave–mean interactions on the internal wave properties will be explored further in a future coherent feature analysis of the same dataset.

c. Topography

Elevated mixing is often observed near the sea floor when strong geostrophic flow or tides interact with rough topography (e.g., Waterman et al. 2013). Here we examine the distribution of dissipation rate and diffusivity near bathymetry using full-depth shipboard CTD profiles from 2013. We use a strain-only parameterization since the LADCP data were not reliable. The average depth in our study region is 5000 m (Fig. 12a) with variations due mainly to small sea mounts (supplemental material 1). Elevated diffusivity is observed near the sea floor especially in the region of the cyclonic eddy (Figs. 12b,c). Although we have only a few full-depth profiles in the cyclonic eddy, the elevated diffusivity is observed almost throughout the water column below 500 m, in agreement with the shear-strain parameterization estimates from the float data.

The mean diffusivity is fairly low throughout the water column $[O(10^{-5})\ \mathrm{m^2\,s^{-1}}]$ except in the bottommost 500 m where it is elevated $[O(10^{-3})\ \mathrm{m^2\ s^{-1}}]$ (Fig. 12b). The overall mean diffusivity of the transect is $3.1 \times 10^{-5}\,\mathrm{m^2\,s^{-1}}$ with a standard deviation of $8.9 \times 10^{-5}\,\mathrm{m^2\,s^{-1}}$. The mean diffusivity in the cyclonic eddy is $4.0 \times 10^{-5}\,\mathrm{m^2\,s^{-1}}$ with $1.7 \times 10^{-4}\,\mathrm{m^2\,s^{-1}}$ in the

bottom 1000 m. The turbulent dissipation rate is also elevated near the bottom and in the upper 1000 m (Fig. 12c). The mean dissipation rate for the region, $5.2 \times 10^{-10}\,m^2\,s^{-3}$ is quite weak with a standard deviation of $7.6 \times 10^{-11}\,m^2\,s^{-3}$. The cyclonic eddy has a mean dissipation rate of $1.6 \times 10^{-10}\,m^2\,s^{-3}$ with a standard deviation of $1.3 \times 10^{-10}\,m^2\,s^{-3}$ in the bottom 1000 m. A more detailed breakdown is given in Table 4. The average diffusivity at different depths is discussed in section 7a.

The southeast Indian Ocean does not require large dissipation of turbulent kinetic energy to maintain the abyssal mixing since this basin is weakly stratified (Sloyan 2006; Nikurashin and Ferrari 2011). Sloyan (2006) found high mixing rates near topographic features in the basin with weak values over plains. Interaction of geostrophic flow and tides with topography can result in elevated diffusivity near the bottom. The former will generate internal lee waves and the latter results in the generation of internal tides with tidal frequency. Among the various tidal components, the barotropic M_2 tidal component contributes around two-thirds of the total global dissipation (Cartwright and Ray 1991). However, the southeast Indian Ocean is a region of weak tides with a mean M_2 amplitude of −0.2 cm (Shriver et al. 2014) and weak tidal energy dissipation compared to the western Indian Ocean (Egbert and Ray 2000). Moreover, the energy conversion of the M_2 component into internal tides in the southeast Indian Ocean is weak to moderate over rough topography (Nycander 2005; Nikurashin and Ferrari 2013). Although it is a region of high eddy kinetic energy, the energy flux going into lee waves is quite weak compared to regions like the Antarctic Circumpolar Current (Nikurashin and Ferrari 2011, 2013). The smaller topographic roughness of the region and the absence of strong geostrophic flow (Nikurashin and Ferrari 2011) could be the reason behind this.

We further pulled out an energy flux (E) of $3.2 \times 10^{-4}\,W\,m^{-2}$ into internal tides and $1.6 \times 10^{-5}\,W\,m^{-2}$ into lee waves for the southeast Indian Ocean from the global maps of Melet et al. (2014). We simply take these estimates as amount of energy available for mixing in the deep ocean from tides and lee waves and estimate a dissipation rate, $\varepsilon = E/(\rho \times \text{depth})$, where $\rho = 1027.8\,kg\,m^{-3}$ (Alford et al. 2012). If these fluxes evenly dissipate over the bottom 1000 m, it would give a very moderate dissipation rate of $3.1 \times 10^{-10}\,m^2\,s^{-3}$ from internal tides and $1.5 \times 10^{-11}\,m^2\,s^{-3}$ from lee waves. The tidal derived dissipation rate has the same order of magnitude as that of the strain-only parameterization estimate from this study for the bottom 1000 m ($1.5 \times 10^{-10}\,m^2\,s^{-3}$). We also compared the few good profiles of LADCP velocity with barotropic tidal velocities predicted from a TPXO7.2 global tidal model. The tidal velocity is close in magnitude to that of the LADCP velocity near the sea floor except in the strong velocity region of cyclonic eddy in the upper 1500 m (Fig. 2 in the online supplemental material). This suggests that the contribution from internal tides could be more important than that from lee waves in providing the required energy to maintain the deep ocean mixing in this region.

TABLE 4. Mean and one standard deviation of dissipation rate ($m^2\,s^{-3}$) and diffusivity ($m^2\,s^{-1}$) at different depth ranges from all three EM-APEX floats in both cyclonic (CE) and anticyclonic (AE) eddies.

Depth	Dissipation rate			Diffusivity		
	EM-6662	EM-6663	EM-6664	EM-6662	EM-6663	EM-6664
250–350-m AE	—	$(19.9 \pm 2.6) \times 10^{-10}$	$(2.8 \pm 0.9) \times 10^{-9}$	—	$(10.2 \pm 0.9) \times 10^{-6}$	$(1.5 \pm 0.4) \times 10^{-5}$
250–350-m CE	$(17.3 \pm 6.4) \times 10^{-10}$	$(10.1 \pm 1.6) \times 10^{-10}$	$(13.1 \pm 2.6) \times 10^{-10}$	$(10.6 \pm 3.5) \times 10^{-6}$	$(6.3 \pm 0.7) \times 10^{-6}$	$(10 \pm 1.9) \times 10^{-6}$
250–350-m all	$(17.8 \pm 6.5) \times 10^{-10}$	$(14.3 \pm 4) \times 10^{-10}$	$(12.6 \pm 6.3) \times 10^{-10}$	$(10.9 \pm 3.7) \times 10^{-6}$	$(8.5 \pm 2.3) \times 10^{-6}$	$(10.1 \pm 4.7) \times 10^{-6}$
250–1000-m AE	—	$(7.3 \pm 4.8) \times 10^{-10}$	$(9.1 \pm 6.1) \times 10^{-10}$	—	$(7.3 \pm 1.9) \times 10^{-6}$	$(9.2 \pm 4.1) \times 10^{-6}$
250–1000-m CE	$(1.7 \pm 2.6) \times 10^{-9}$	$(4.8 \pm 1.8) \times 10^{-10}$	$(1.8 \pm 2.1) \times 10^{-9}$	$(3.1 \pm 5.3) \times 10^{-5}$	$(5.9 \pm 1.4) \times 10^{-6}$	$(3.3 \pm 5.2) \times 10^{-5}$
250–1000-m all	$(1.7 \pm 2.6) \times 10^{-9}$	$(5.7 \pm 3.3) \times 10^{-10}$	$(7.9 \pm 10.8) \times 10^{-10}$	$(3.1 \pm 5.2) \times 10^{-5}$	$(6.5 \pm 1.7) \times 10^{-6}$	$(1.3 \pm 2.5) \times 10^{-5}$
SAMW AE	—	$(4.1 \pm 0.9) \times 10^{-10}$	$(3.7 \pm 0.9) \times 10^{-10}$	—	$(6.2 \pm 1.4) \times 10^{-6}$	$(5.7 \pm 1.8) \times 10^{-6}$
SAMW CE	$(13.6 \pm 4.1) \times 10^{-10}$	$(3.6 \pm 0.8) \times 10^{-10}$	$(11.1 \pm 1.6) \times 10^{-10}$	$(10.3 \pm 6.5) \times 10^{-6}$	$(5.4 \pm 0.7) \times 10^{-6}$	$(11.8 \pm 2.4) \times 10^{-6}$
SAMW all	$(13.9 \pm 4.0) \times 10^{-10}$	$(3.4 \pm 0.8) \times 10^{-10}$	$(4.7 \pm 1.1) \times 10^{-10}$	$(10.5 \pm 6.3) \times 10^{-6}$	$(5.4 \pm 1.1) \times 10^{-6}$	$(7.5 \pm 1.8) \times 10^{-6}$
AAIW AE	—	$(4.2 \pm 0.5) \times 10^{-10}$	$(7.6 \pm 1.9) \times 10^{-10}$	—	$(7.2 \pm 0.6) \times 10^{-6}$	$(11.3 \pm 2.5) \times 10^{-6}$
AAIW CE	$(2.5 \pm 2.6) \times 10^{-9}$	$(4.9 \pm 0.5) \times 10^{-10}$	$(2.2 \pm 1.7) \times 10^{-9}$	$(4.7 \pm 5) \times 10^{-5}$	$(6.3 \pm 0.7) \times 10^{-6}$	$(4.2 \pm 3.6) \times 10^{-5}$
AAIW all	$(2.5 \pm 2.5) \times 10^{-9}$	$(4.8 \pm 0.5) \times 10^{-10}$	$(8.9 \pm 8.5) \times 10^{-10}$	$(4.6 \pm 4.9) \times 10^{-5}$	$(7.1 \pm 0.8) \times 10^{-6}$	$(1.4 \pm 1.7) \times 10^{-5}$

7. Discussion

a. Comparison between different datasets

To validate the finescale parameterization of dissipation, we compare the float estimates with direct measurements from the

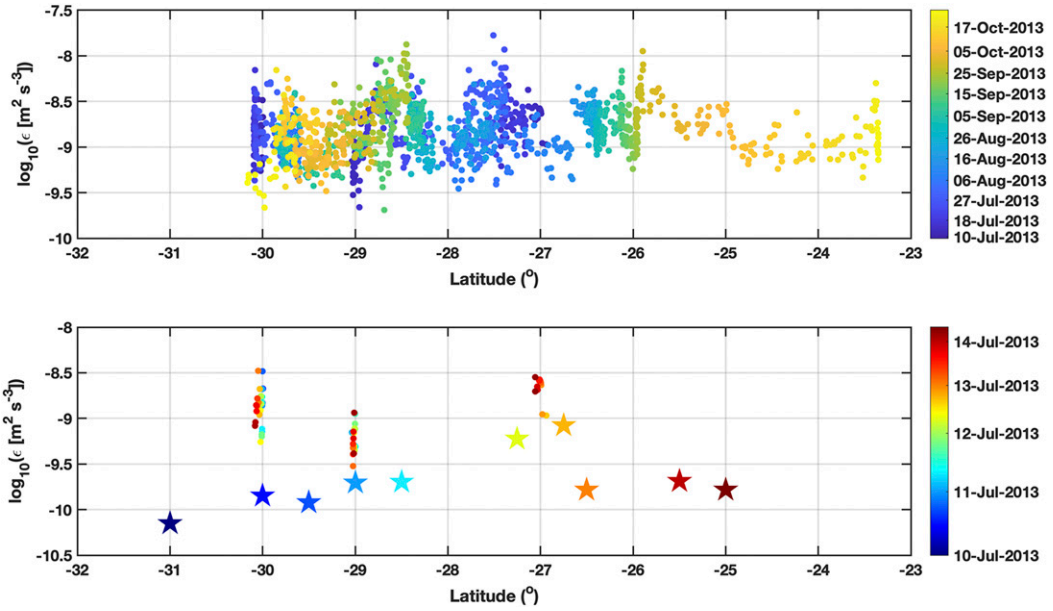

FIG. 13. (top) Depth-averaged dissipation rate estimates between 240 and 300 m from floats as a function of latitude and time. (bottom) Depth-averaged dissipation rate from floats (circles) and VMP (stars) for the same depth range during the five days of VMP measurements in 2013. The color represents time in both panels. Note the difference in the color axis for both panels.

VMP taken on the same voyage. The parameterization operates at larger length and time scales with the assumption of internal wave–driven mixing, whereas the VMP directly measures the centimeter-scale turbulence. The VMP measurement is a snapshot of turbulence at an instant, which may be only partly caused by internal wave breaking. The finescale parameterization provides the average dissipation rate over several wave periods (Whalen et al. 2015). Nevertheless, it is useful to compare the finescale parameterization estimates with VMP measurements at the depths where they overlap.

We collected 1566 profiles from the EM-APEX floats during July–October 2013 and only 18 VMP profiles between 10 and 14 July 2013 (Fig. 1c). The depth-averaged float estimates in the upper 300 m show large spatial and temporal variability (Fig. 13, top). The floats covered about 7° of latitude in four months. During this time, the float estimates vary by about two orders of magnitude. The VMP measurements only extend to 300 m, whereas the parameterization from the floats begins at 240 m. There are only 10 VMP profiles that cover this depth range (Fig. 5c). The depth-averaged values of float estimates and VMP measurements at this depth range that are less than five days apart in time are within an order of magnitude (Fig. 13, bottom). Figure 13 gives a comparison between the finescale parameterization and VMP dissipation rate measurements profile by profile. Despite all the spatial and temporal variability as well as the sampling differences and uncertainties from the parameterization due to assumptions in these estimates, overall, the float estimates are in decent agreement with the VMP measurements that are close in space and time. For instance, we have fairly good agreement at latitudes of 27°S, whereas an order of magnitude difference at 30°S. This gives us some confidence that the float estimates are robust. The mean vertical profile of the parameterization estimates from the floats overestimates the mean vertical profile of VMP measurements in the depth range where they overlap between 200 and 300 m (Fig. 13).

TABLE 5. Mean diffusivity ($m^2\,s^{-1}$) and one standard deviation at different depth ranges from floats (shear–strain), shipboard data (strain-only), and VMP in the southeast Indian Ocean in 2012 and 2013.

Depth	Shear–strain	Strain-only	VMP
Surface–300 m	—	—	$1.5 \times 10^{-4} \pm 0.002$ (2012)
			$4.0 \times 10^{-4} \pm 0.007$ (2013)
240–300 m	$(11 \pm 2.3) \times 10^{-6}$ (2013)	—	$(2.4 \pm 1.6) \times 10^{-7}$ (2013)
250–500 m	$(8.5 \pm 1.3) \times 10^{-6}$ (2013)	$(9.3 \pm 1.4) \times 10^{-6}$ (2012)	—
		$(10 \pm 3) \times 10^{-6}$ (2013)	—
500–1000 m	$(2.1 \pm 2.8) \times 10^{-5}$ (2013)	$(14 \pm 4) \times 10^{-6}$ (2012)	—
		$(15 \pm 7) \times 10^{-6}$ (2013)	—
1000 m–bottom	—	$(3.5 \pm 9.7) \times 10^{-5}$ (2013)	—

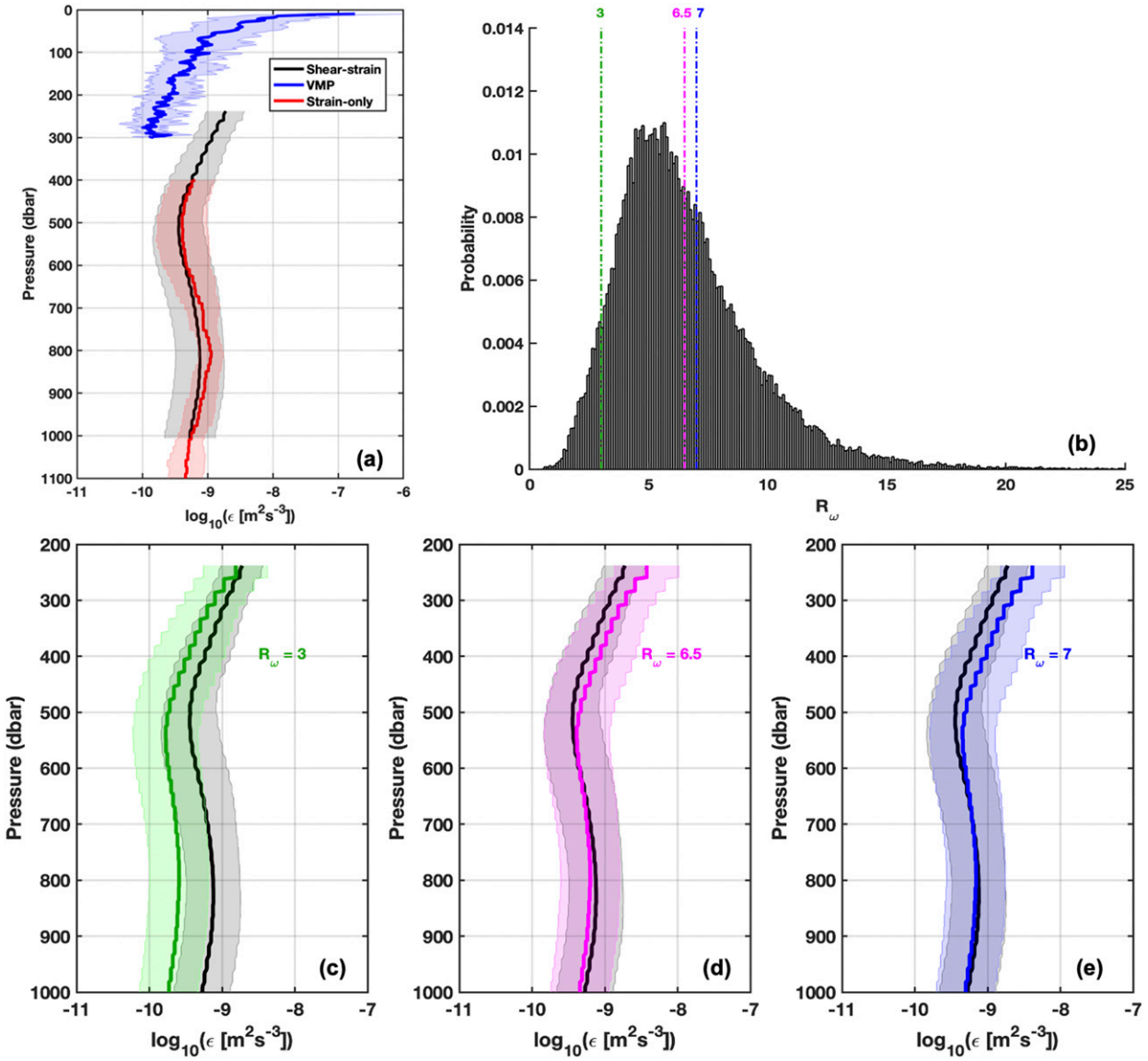

FIG. 14. (a) Mean depth profile of dissipation rate in the upper 1100 m estimated from all float profiles using shear–strain method (black), shipboard data using strain-only method (red) and VMP measurements (blue). (b) The histogram of R_ω from the floats with the values used for the strain-only estimations (bottom panels) are marked with colored vertical dashed lines. Mean vertical profiles of dissipation rate from shear-strain parameterization (black) and (c) strain-only parameterization with $R_\omega = 3$ (green; Whalen et al. 2012), (d) strain-only parameterization with $R_\omega = 6.5$ (pink, float mean), and (e) strain-only parameterization with $R_\omega = 7$ (blue; Kunze et al. 2006). The shading represents one standard deviation.

The large temporal and spatial variability of the float data could be one of the reasons behind the overestimation.

Finescale predictions of dissipation from the shear–strain method (e.g., Gregg 1989; Polzin et al. 1995; Sheen et al. 2013; Waterman et al. 2013) and strain-only method (e.g., Wijesekera et al. 1993; Whalen et al. 2012) typically agree within a factor of 2–3 with the microstructure measurements. However, the finescale estimates can overpredict the microstructure values up to a factor of 8 in the bottommost 500–1000 m (e.g., Sheen et al. 2013; Waterman et al. 2013) in regions of rough topography and strong bottom flow. Here we compare the depth-averaged diffusivities from all datasets at different depth ranges (Table 5). Overall, the estimated diffusivity is weak [$O(10^{-6})$ m^2 s^{-1}] at depths from 250 to 1000 m in agreement with Waterhouse et al. (2014) except in regions of cyclonic eddies. Below 1000-m depth, the dissipation rate decreases rapidly with depth and the diffusivity is nearly constant with depth. This suggests that less internal wave dissipation is available below 1000 m, in agreement with Huussen et al. (2012). Near the boundaries, elevated dissipation rate and diffusivity is observed in both direct and parameterized estimates. The finescale parameterization has a mean diffusivity of 11×10^{-6} m^2 s^{-1} in the upper 240–300 m, whereas the VMP

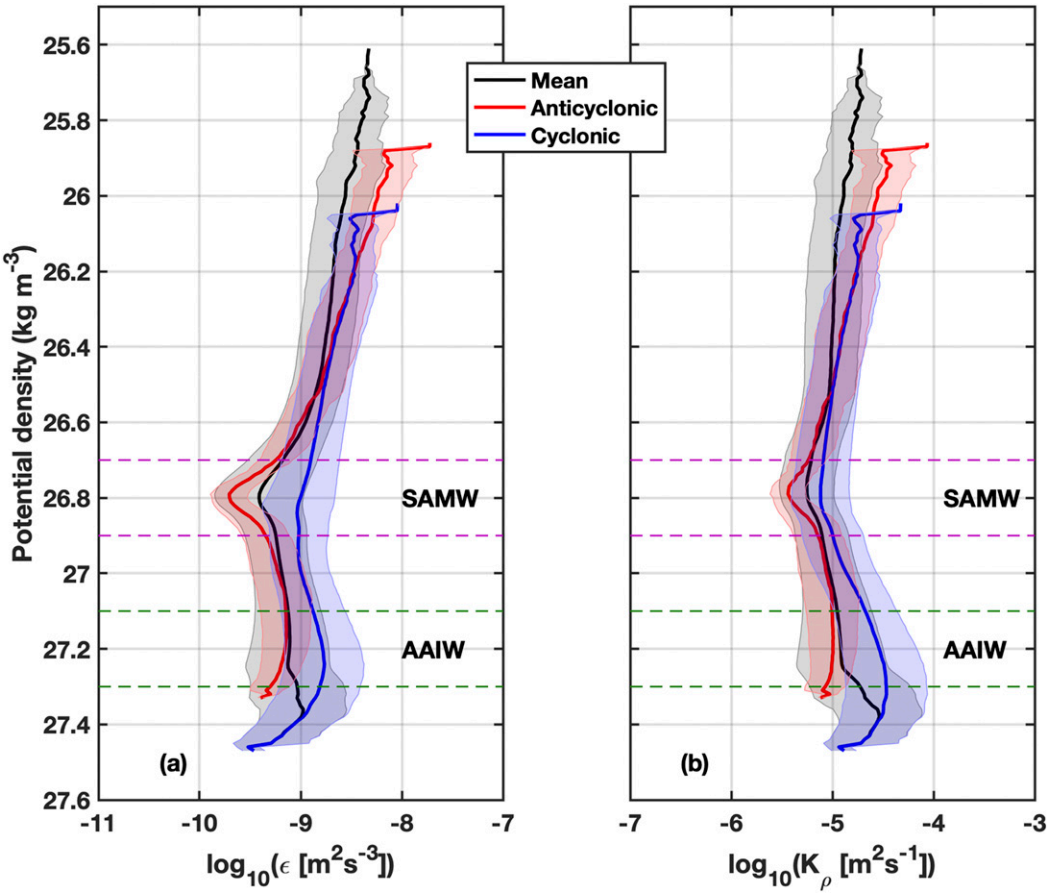

FIG. 15. Mean profiles of (a) dissipation rate and (b) diffusivity from the floats in anticyclonic eddies (red line), cyclonic eddies (blue line) and for the full float data (black line) plotted on a vertical axis of potential density relative to the sea surface. The density range for SAMW and AAIW are marked. The color shading is one standard deviation.

has a mean of $1.9 \times 10^{-4}\,\mathrm{m^2\,s^{-1}}$ in the upper 300 m. The strain parameterization has diffusivities that are of similar magnitude within the depth ranges of 250–500 and 500–1000 m.

The parameterization estimates are sensitive to the magnitude of R_ω with higher dissipation observed for smaller values of R_ω (Polzin et al. 1995). Strain-only parameterization has been widely used since strain (density) measurements are comparatively easy to obtain (Whalen et al. 2012, 2015, 2018; Sloyan 2005). However, this requires the assumption of a constant value for R_ω. In this study, the R_ω value for the strain-only parameterization ($R_\omega = 6$) is chosen from the observed R_ω values from float profiles closer in space and time to the shipboard CTD measurements (Fig. 13). This resulted in shear-strain estimates from the floats and the strain-only estimates from the shipboard data that are in good agreement (Fig. 14a), both qualitatively and quantitatively. Whalen et al. (2012) used a constant R_ω of 3 and estimated the distribution of diffusivity globally. They found diffusivity one order higher than our estimates for the southeast Indian Ocean. Our estimates are of the same order of magnitude as that of Waterhouse et al. (2014) where they estimated diffusivity from microstructure profilers and shear–strain parameterization.

We further investigated the sensitivity of dissipation rate estimates to the choice of R_ω using the float data (Figs. 14c–e). For the float data, R_ω varies between 1 and 25 with a mean value of 6.5 (Fig. 14b). We estimated the dissipation rates from strain-only parameterization with $R_\omega = 3$ (Whalen et al. 2012), $R_\omega = 7$ (Kunze et al. 2006) and the float mean of 6.5 and compared it with the dissipation rate from shear-strain parameterization. The estimates using $R_\omega = 6.5$ and 7 differs by a factor of 2 above 500 m with that from the shear–strain estimates. Below 500 m, the two strain-only profiles are very similar to the shear–strain parameterization profile (Figs. 14d,e). The choice of $R_\omega = 3$ results in a significantly smaller dissipation rates than the shear-strain parameterization dissipation rate estimates, particularly below 500-m depth. This difference is sensitive to the high wavenumber integration limits for the shear-strain spectra and can differ by an order of magnitude for a limit of 12 and 25 m. Thus, we suggest that $R_\omega = 7$ is a much better choice than $R_\omega = 3$ for strain-only estimations in this region. In addition, the vertical distribution of dissipation rate and diffusivity from our strain parameterization using shipboard CTD data (Fig. 12) matches with the average Indian Ocean profiles in Kunze et al. (2006) using a R_ω value of 7

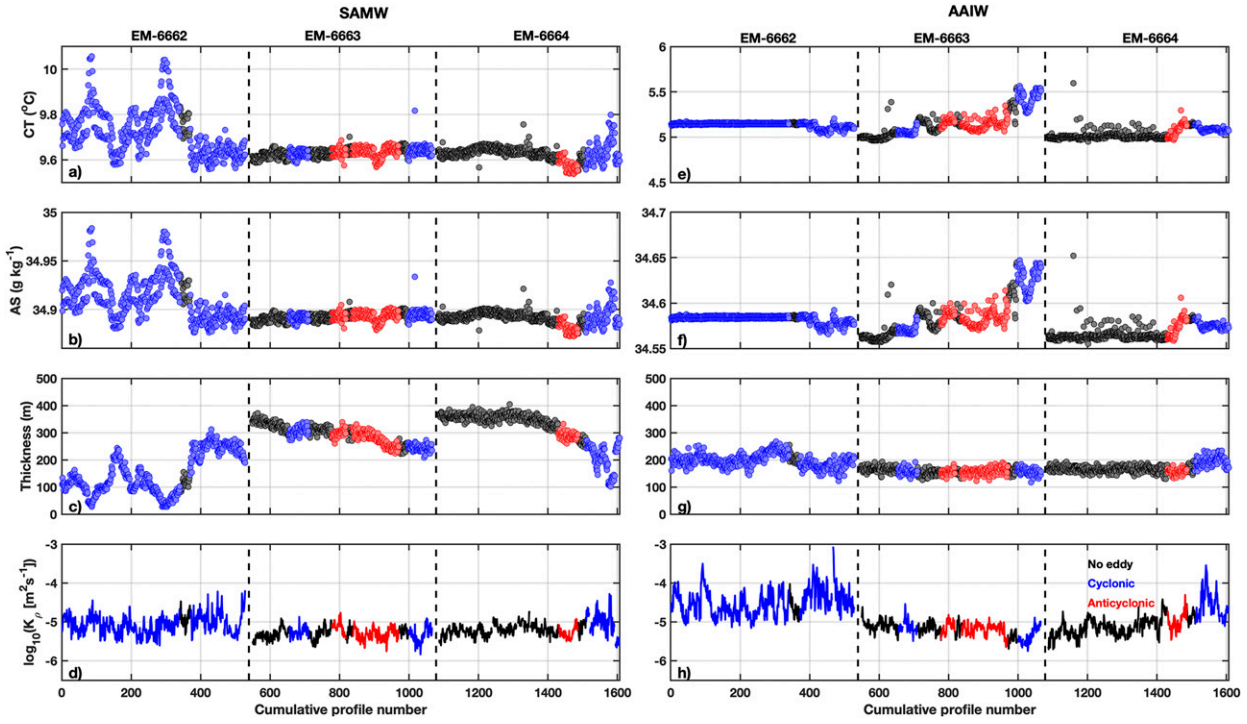

FIG. 16. Mean of (a) Conservative Temperature, (b) Absolute Salinity, (c) thickness, and (d) diffusivity in the SAMW layer along the float tracks. (e)–(h) As in (a)–(d), but for the AAIW layer. The black circles represent profiles in noneddy regions, and red (blue) circles represent profiles in anticyclonic (cyclonic) eddies.

with a strain-only parameterization. Their strain-only diffusivity estimates agreed with shear-strain parameterized estimates to within a factor of 2. From this we conclude that diffusivity estimates are greatly improved by velocity observations that allow the use of shear–strain parameterization and no assumption of R_ω.

b. *Impact on water masses and large-scale circulation*

The main middepth water masses in the subtropical Indian Ocean are the SAMW and AAIW. SAMW in the Indian Ocean, forms between the subtropical front (STF) and the Subantarctic Front (SAF) south of Australia and is advected westward to enter, and ventilate, the subtropical gyre (Sallée et al. 2006). The AAIW that enters the Indian Ocean originates from the southwestern Atlantic and is substantially modified (higher salinity and PV) by the time it enters the Indian Ocean (Talley 2011). Both AAIW and SAMW are an integral part of the global overturning circulation as well as global heat, freshwater, and carbon budgets (Sloyan et al. 2010).

Turbulent mixing due to internal wave breaking plays an important role in the deep ocean water-mass transformation and thereby controls the global overturning circulation (Nikurashin and Ferrari 2013). From the float data in the upper 200–1000 m, we observe higher dissipation and mixing at depths corresponding to AAIW in the potential density range of 27.1–27.3 kg m^{-3} (Fig. 15). The dissipation rate and diffusivity in cyclonic eddies peak at potential density 27.3 kg m^{-3}. In anticyclonic eddies, higher dissipation and diffusivity is observed near the surface with weak mixing in the layers of SAMW and AAIW. Minimum dissipation rate and diffusivity is observed within the SAMW layer at potential density 26.8 kg m^{-3}. The SAMW layer has a weaker dissipation rate of 7.4×10^{-10} m^3 s^{-2} and diffusivity of 7.8×10^{-6} m^2 s^{-1}. The AAIW layer has a mean dissipation rate of 1.3×10^{-9} m^2 s^{-3} and diffusivity of 2.3×10^{-5} m^2 s^{-1}. We found that the cyclonic eddies elevate the diffusivity in both AAIW and SAMW layers, whereas the weakest mixing values in SAMW and AAIW are found within anticyclonic eddies (Fig. 15). Thus, most of the mixing in our study region takes place within the AAIW layer, with much lower mixing rates in the SAMW.

We have demonstrated that both cyclonic and anticyclonic eddies play an important role in modifying turbulent mixing. Thus, the water-mass transformation in the southeast Indian Ocean, will be strongly affected by the mesoscale eddies in this highly energetic region. Whalen et al. (2018) found regions of anticyclonic vorticity was associated with elevated internal wave–driven mixing in the upper 250–500 m. This was not the case for cyclonic vorticity regions. In our study, elevated mixing was found below 500 m in cyclonic eddies that are subsurface intensified. This study suggests that the interactions between internal waves and cyclonic eddies may impact the water-mass transformation below 500 m in this region.

Water-mass transformation within the SAMW and AAIW layers was further explored by plotting the mean properties of each layer along the float trajectories (Fig. 16). The temperature and salinity of SAMW is elevated within cyclonic eddies

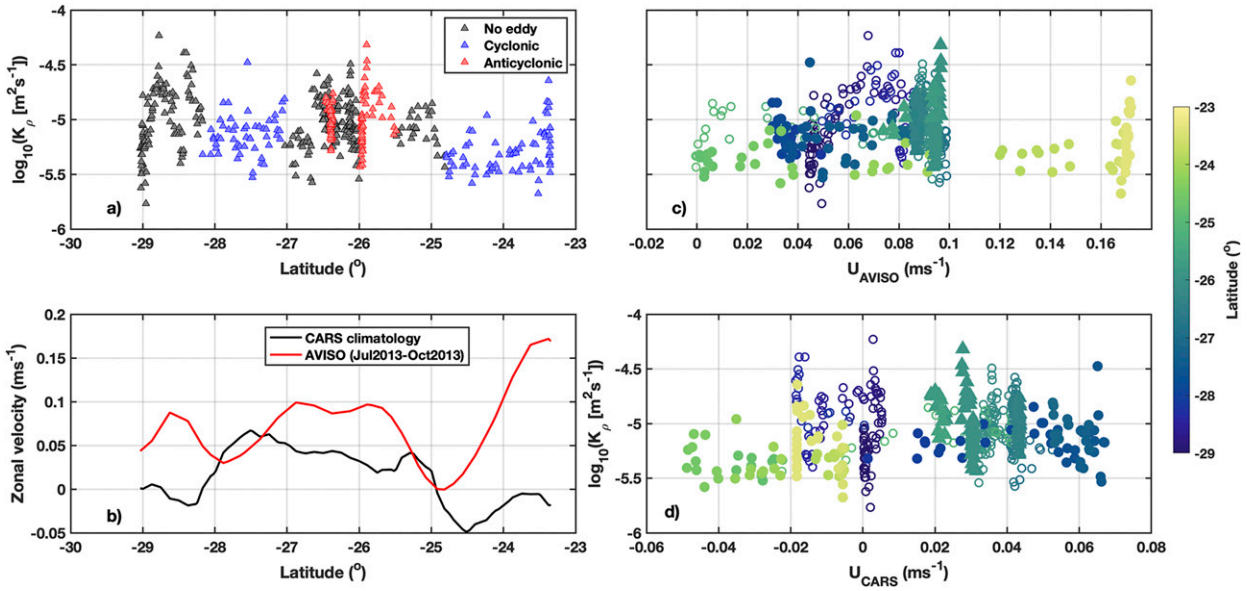

FIG. 17. (a) Depth-averaged diapycnal diffusivity in the upper 300 m along the track of float EM-6663, which covered the widest latitudinal band. The estimates in cyclonic (blue) and anticyclonic (red) eddies are marked. (b) The annual mean zonal geostrophic velocity from the CARS climatology between 100° and 105°E in the upper 200 m (black line) and the mean surface geostrophic velocity from AVISO (red line) between 100° and 105°E during the time of float profiling. Scatterplot of depth-averaged diffusivity in the upper 300 m plotted against (c) surface geostrophic velocity and (d) annual mean eastward velocity from CARS in the upper 200 m. Data points in (c) and (d) are colored by latitude. Open circles correspond to profiles in noneddy region and filled circles (triangles) correspond to profiles in cyclonic (anticyclonic) eddies.

(EM-6662, Figs. 16a,b) where the SAMW layer has reduced thickness (Fig. 16c, Figs. 3 and 4). Water properties are less influenced by the anticyclonic eddies where the SAMW layer lies well below 300 m (EM-6663 and EM-6664). The mean diffusivity within the SAMW layer is of the $O(10^{-6})$ $m^2 s^{-1}$ (Fig. 16d). We find no linear relationship between diffusivity and SAMW layer thickness, however, diffusivity in regions of cyclonic vorticity in EM-6662 is higher compared to the noneddy regions of EM-6663 and EM-6664 (Fig. 16d). This suggests that in regions of cyclonic eddies where the thickness of SAMW layer is very low, the warm and salty STUW lying above might be mixing with the SAMW at the interface and modifying its properties.

In contrast to the SAMW layer, the properties of the AAIW layer are less affected by the cyclonic eddies CE1 and CE2 in EM-6662 and EM-6664 (Figs. 16e,f). This is counterintuitive since turbulent mixing is higher in regions of AAIW, and higher still inside cold core eddies, while weaker mixing is found in the SAMW layer where water-mass modification is strong. (Tables 3 and 4). EM-6663, which followed a roughly meridional path northward (Fig. 1e), experienced a gradual increase in AAIW temperature and salinity consistent with the large-scale circulation and erosion of property extrema with increasing distance from the source (Talley 2011). A temperature–salinity plot of this float shows a progression to warmer and saltier properties in the AAIW density layer as the float moves northward, recording the transition from AAIW to the warmer, saltier Indonesian Intermediate Water that occupies the same density range (not shown). Unlike the SAMW layer, the thickness of the AAIW layer is almost constant (~200 m) irrespective of the presence of eddies (Fig. 16g). The mean diffusivity of the layer is high within cyclonic eddies as we have seen earlier (Fig. 16h).

Internal wave breaking can feed back on the large-scale circulation and thereby climate (Garrett 2003). Enhanced mixing in the upper water column is often attributed to the breaking of near-inertial internal waves generated due to wind forcing and also by the trapping of these waves in anticyclonic eddies. We have seen that the internal waves and eddies interact and now turn briefly to consider potential interaction between the SICC and mixing due to breaking internal waves. From the high-resolution (1/8°) CSIRO Atlas of Regional Seas (CARS09) hydrographic climatology of geostrophic velocities, the southern branch of the SICC (sSICC) is represented as a broad jet between 25° and 29°S at 105°E (Fig. 17b, black line). The average surface zonal geostrophic velocity from AVISO altimetry during the float profiling shows three jets near 28.5°S, 26°–27°S, and 23°–24°S (Fig. 17b, red line). Figure 17 examines the relationship between mean surface zonal velocities and depth-averaged diffusivity. There is no direct relationship, however, profiles in anticyclonic eddies show elevated diffusivity in regions of the sSICC near 27°S. Diffusivity is also elevated in noneddy regions where the zonal velocity magnitudes correspond to that of the SICC jet (Fig. 17b). This suggests that the internal-wave-driven mixing in the upper ocean may be contributed by instabilities of the SICC branches and the mixing may in turn impact the evolution of the SICC branches.

8. Conclusions

We analyzed the spatial and temporal variability of turbulent mixing in the southeast Indian Ocean for the first time using data collected from EM-APEX profiling floats, shipboard CTD, and microstructure profilers. Elevated diffusivity is observed near the surface in agreement with wind generation and downward propagation of near-inertial internal waves. Most of the observed mixing variability below the mixed layer is associated with mesoscale eddies and/or bottom topography. We observe elevated mixing in anticyclonic eddies near the surface consistent with near-inertial wave trapping. Enhanced dissipation is observed in cyclonic eddies below 500 m associated with downward-propagating internal waves. The mean diffusivity in the 250–500 m is of the $O(10^{-6})$ $m^2 s^{-1}$, and it increases to $O(10^{-5})$ $m^2 s^{-1}$ in the 500–1000 m due to elevated diffusivity in cyclonic eddies. Turbulent mixing is weak in the SAMW layer and high in the AAIW layer of cyclonic eddies. However, the properties of SAMW are highly modified in the cyclonic eddies and less affected in the AAIW layer. These results indicate that the deep reaching structure of the cyclonic eddies and the associated current play an important role in internal wave–driven mixing at the intermediate layer and possibly the deep ocean. In addition to these wave–eddy interactions, we found that instabilities of the SICC jet affect diffusivity, highlighting the importance of wave–eddy–mean flow interactions. Our knowledge of mixing variability and its impact on ocean stratification and, therefore, climate variability is extremely limited and requires increased observations of mixing and development of parameterizations for these finescale processes in climate models.

Acknowledgments. We thank the two anonymous reviewers for their insightful comments. A. C. thanks Dr. Amelie Meyer and Dr. Kurt Polzin for the helpful discussions. A. C. also acknowledges the support from Quantitative Marine Science (QMS) program, a joint program between University of Tasmania and CSIRO. H. P. and N. B. acknowledge support from the ARC Discovery Project DP130102088, Australian Government Department of the Environment and Energy National Environmental Science Programme (NESP), and ARC Centre of Excellence in Climate Extremes. This project also received grant funding from the Australian Government (ASCI000002). M. F. acknowledges the support from CSHOR, a joint initiative between the Qingdao National Laboratory for Marine Science and Technology (QNLM), CSIRO, University of New South Wales, and University of Tasmania.

APPENDIX

EM-APEX Float Data Processing

a. Mission

The profiling mission of the floats is a compromise between obtaining the largest possible depth range with a profiling frequency that resolves the inertial cycle, requiring pairs of down-profiles separated by half an inertial period, and similarly for up-profile pairs. The inertial period at 27°S is 26.4 h. This gave eight profiles (four down–up pairs) to 1200-m depth in each inertial period with an average fall/rise rate of 11 cm s^{-1}, allowing the near-inertial and subinertial frequencies in the data to be separated accurately. Although the five floats were deployed across a 7° latitude range, we chose to set identical missions for each float, anticipating that they would migrate substantially during their lifetime.

b. Data return

The five EM-APEX returned a total of 3726 profiles of temperature, salinity, and velocity. After the deployment, two of the floats, EM-6217 and EM-6218, exhibited spikes in the velocity data known to be symptomatic of a high-pressure leak in the float hull (J. Dunlap 2013, personal communication) The maximum pressure was reduced until the spiking disappeared. These two floats continued to profile successfully to 300-m depth for the same period as the three deeper floats, with the added advantage of completing twice the number of profiles per inertial period. The suspected reason for this fault is deterioration in the agar gel protecting the electrodes, as there was about a 12-month period between production and deployment of these two floats. EM-6217 returned 1102 profiles and EM-6218 returned 1058.

Toward the end of the deployment voyage, the profiling mission for the deeper floats was changed to add a drift at 1000-m depth for about 18 h. The drift was added to extend the life of the float but still allow a rapid burst of profiling over an inertial period between drifts. During the drift, the floats measured temperature, salinity, and pressure. Velocity measurements are only possible when a float is moving vertically and rotating around its vertical axis.

c. Quality control and calibration

Occasionally the GPS position of the profile was wrong considering the position of the float at earlier and later profiles. These wrong positions were removed, and the missing locations were linearly interpolated from the profile positions before and after the one in question.

The pressure sensor on the floats may develop a pressure drift with time. The surface pressure for a given profile was subtracted from all pressure values in that profile, effectively resetting the surface pressure to zero. The first pressure in each float record was higher. These values were replaced by the offset value of the adjacent profile.

The EM-APEX temperature, salinity, and pressure measurements are obtained from a Sea Bird Electronics SBE-41 CTD, mounted above the electrodes on the upper end cap. Vertical sample spacing was 2–3 m. The temperature and salinity profiles were compared with the CARS09 (www.cmar.csiro.au/cars) climatology to identify erroneous data and spikes. The climatology was interpolated at each profile location and plotted along with the float measurements and each profile was inspected visually. Occasional spikes were detected and removed. Much of the salinity data from EM-6217 were dominated by extensive spiking and were not used for this study. The cause of the failure may have been related to the high pressure leak described earlier. For all other floats, temperature and salinity measurements are in good agreement with the climatology below 200-m depth where the seasonal and diurnal variability is less. We also checked for drift in the conductivity sensor. No drift was evident in

the data based on examination of salinity on potential temperature surfaces at the deepest common level of each float.

For the calibration of relative velocity measured by the floats and estimation of absolute velocity, we followed the procedure in Phillips and Bindoff (2014). The steps involved are as follows:

- Calibrate the angle between the electrode axes and the compass orientation.
- Remove all the velocity spikes using a depth-dependent cut off based on a statistical analysis of the RMS error velocity. For velocities above 100 m, we excluded values greater than 2 cm s^{-1}.
- Estimate the absolute velocity from the float-measured relative velocities by adding a depth-independent offset, which is equivalent to the depth-averaged absolute velocity from the sea surface to the sea floor (Sanford 1971). The offset is calculated as the difference between the displacement due to the measured relative velocities along a path from the surface to the bottom of a down profile and back to the surface, and the actual displacement of the float measured by GPS.

We then interpolated the temperature, salinity, and velocity measurements onto a uniform pressure grid of 3 dbar before the analysis.

REFERENCES

Alford, M. H., 2003: Improved global maps and 54-year history of wind-work on ocean inertial motions. *Geophys. Res. Lett.*, **30**, 1424, https://doi.org/10.1029/2002GL016614.

——, M. F. Cronin, and J. M. Klymak, 2012: Annual cycle and depth penetration of wind-generated near-inertial internal waves at Ocean Station Papa in the northeast Pacific. *J. Phys. Oceanogr.*, **42**, 889–909, https://doi.org/10.1175/JPO-D-11-092.1.

Amante, C., and B. Eakins, 2009: ETOPO1 Global Relief Model converted to PanMap layer format. NOAA/National Geophysical Data Center, accessed 21 June 2017, https://doi.org/10.1594/PANGAEA.769615.

Balmforth, N. J., and W. R. Young, 1999: Radiative damping of near-inertial oscillations in the mixed layer. *J. Mar. Res.*, **57**, 561–584, https://doi.org/10.1357/002224099321549594.

Benthuysen, J., R. Furue, J. P. McCreary, N. L. Bindoff, and H. E. Phillips, 2014: Dynamics of the Leeuwin Current: Part II. Impacts of mixing, friction, and advection on a buoyancy-driven eastern boundary current over a shelf. *Dyn. Atmos. Oceans*, **65**, 39–63, https://doi.org/10.1016/j.dynatmoce.2013.10.004.

Birol, F., and R. Morrow, 2001: Source of the baroclinic waves in the southeast Indian Ocean. *J. Geophys. Res.*, **106**, 9145–9160, https://doi.org/10.1029/2000JC900044.

Bray, N. A., and N. P. Fofonoff, 1981: Available potential-energy for MODE eddies. *J. Phys. Oceanogr.*, **11**, 30–47, https://doi.org/10.1175/1520-0485(1981)011<0030:APEFME>2.0.CO;2.

Bryan, F., 1987: Parameter sensitivity of primitive equation ocean general circulation models. *J. Phys. Oceanogr.*, **17**, 970–985, https://doi.org/10.1175/1520-0485(1987)017<0970:PSOPEO>2.0.CO;2.

Bühler, O., and E. McIntyre, 2005: Wave capture and wave-vortex duality. *J. Fluid Mech.*, **534**, 67–95, https://doi.org/10.1017/S0022112005004374.

Cairns, J. L., and G. O. Williams, 1976: Internal wave observations from a midwater float, 2. *J. Geophys. Res.*, **81**, 1943–1950, https://doi.org/10.1029/JC081i012p01943.

Cartwright, D. E., and R. D. Ray, 1991: Energetics of global ocean tides from Geosat altimetry. *J. Geophys. Res.*, **96**, 16 897–16 912, https://doi.org/10.1029/91JC01059.

Chinn, B. S., J. B. Girton, and M. H. Alford, 2016: The impact of observed variations in the shear-to-strain ratio of internal waves on inferred turbulent diffusivities. *J. Phys. Oceanogr.*, **46**, 3299–3320, https://doi.org/10.1175/JPO-D-15-0161.1.

Cyriac, A., M. McPhaden, H. Phillips, N. Bindoff, and M. Feng, 2019: Seasonal evolution of the surface layer heat balance in the eastern subtropical Indian Ocean. *J. Geophys. Res. Oceans*, **124**, 6459–6477, https://doi.org/10.1029/2018JC014559.

D'Asaro, E. A., 1985: The energy flux from the wind to near-inertial motions in the surface mixed layer. *J. Phys. Oceanogr.*, **15**, 1043–1059, https://doi.org/10.1175/1520-0485(1985)015<1043:TEFFTW>2.0.CO;2.

de Boyer Montegut, C., G. Madec, A. S. Fischer, A. Lazar, and D. Iudicone, 2004: Mixed layer depth over the global ocean: An examination of profile data and a profile-based climatology. *J. Geophys. Res.*, **109**, C12003, https://doi.org/10.1029/2004JC002378.

Dillon, T. M., and D. R. Caldwell, 1980: The Batchelor spectrum and dissipation in the upper ocean. *J. Geophys. Res.*, **85**, 1910–1916, https://doi.org/10.1029/JC085iC04p01910.

——, J. G. Richman, C. G. Hansen, and M. D. Pearson, 1981: Near-surface turbulence measurements in a lake. *Nature*, **290**, 390–392, https://doi.org/10.1038/290390a0.

Divakaran, P., and G. B. Brassington, 2011: Arterial ocean circulation of the southeast Indian Ocean. *Geophys. Res. Lett.*, **38**, L01802, https://doi.org/10.1029/2010GL045574.

Domingues, C. M., M. E. Maltrud, S. E. Wijffels, J. A. Church, and M. Tomczak, 2007: Simulated Lagrangian pathways between the Leeuwin Current system and the upper-ocean circulation of the southeast Indian Ocean. *Deep-Sea Res. II*, **54**, 797–817, https://doi.org/10.1016/j.dsr2.2006.10.003.

Egbert, G. D., and R. D. Ray, 2000: Significant dissipation of tidal energy in the deep ocean inferred from satellite altimeter data. *Nature*, **405**, 775–778, https://doi.org/10.1038/35015531.

Feng, M., S. Wijffels, S. Godfrey, and G. Meyers, 2005: Do eddies play a role in the momentum balance of the Leeuwin Current? *J. Phys. Oceanogr.*, **35**, 964–975, https://doi.org/10.1175/JPO2730.1.

Furue, R., K. Guerreiro, H. E. Phillips, J. McCreary, P. Julian, and N. L. Bindoff, 2017: On the Leeuwin Current System and its linkage to zonal flows in the south Indian Ocean as inferred from a gridded hydrography. *J. Phys. Oceanogr.*, **47**, 583–602, https://doi.org/10.1175/JPO-D-16-0170.1.

Garabato, A. C. N., K. L. Polzin, B. A. King, K. J. Heywood, and M. Visbeck, 2004: Widespread intense turbulent mixing in the Southern Ocean. *Science*, **303**, 210–213, https://doi.org/10.1126/science.1090929.

Garrett, C., 2003: Mixing with latitude. *Nature*, **422**, 477–478, https://doi.org/10.1038/422477a.

Godfrey, J. S., and K. R. Ridgway, 1985: The large-scale environment of the poleward-flowing Leeuwin Current, Western Australia: Longshore steric height gradients, wind stresses and geostrophic flow. *J. Phys. Oceanogr.*, **15**, 481–495, https://doi.org/10.1175/1520-0485(1985)015<0481:TLSEOT>2.0.CO;2.

Greenan, B. J., N. S. Oakey, and F. W. Dobson, 2001: Estimates of dissipation in the ocean mixed layer using a quasi-horizontal microstructure profiler. *J. Phys. Oceanogr.*, **31**, 992–1004, https://doi.org/10.1175/1520-0485(2001)031<0992:EODITO>2.0.CO;2.

Gregg, M. C., 1989: Scaling turbulent dissipation in the thermocline. *J. Geophys. Res.*, **94**, 9686–9698, https://doi.org/10.1029/JC094iC07p09686.

——, T. B. Sanford, and D. P. Winkel, 2003: Reduced mixing from the breaking of internal waves in equatorial waters. *Nature*, **422**, 513–515, https://doi.org/10.1038/nature01507.

——, E. A. D'Asaro, J. J. Riley, and E. Kunze, 2018: Mixing efficiency in the ocean. *Annu. Rev. Mar. Sci.*, **10**, 443–473, https://doi.org/10.1146/annurev-marine-121916-063643.

Hanawa, K., and L. D. Talley, 2001: Mode waters. *Ocean Circulation and Climate: Observing and Modelling the Global Ocean*, G. Siedler, J. Church, and J. Gould, Eds., International Geophysics Series, Vol. 77, Elsevier, 373–386.

Harrison, M. J., and R. W. Hallberg, 2008: Pacific subtropical cell response to reduced equatorial dissipation. *J. Phys. Oceanogr.*, **38**, 1894–1912, https://doi.org/10.1175/2008JPO3708.1.

Henyey, F. S., J. Wright, and S. M. Flatte, 1986: Energy and action flow through the internal wave field: An eikonal approach. *J. Geophys. Res.*, **91**, 8487–8495, https://doi.org/10.1029/JC091iC07p08487.

Huussen, T. N., A. C. Naveira-Garabato, H. L. Bryden, and E. L. McDonagh, 2012: Is the deep Indian Ocean MOC sustained by breaking internal waves? *J. Geophys. Res.*, **117**, C08024, https://doi.org/10.1029/2012JC008236.

Jia, F., L. Wu, and B. Qiu, 2011: Seasonal modulation of eddy kinetic energy and its formation mechanism in the southeast Indian Ocean. *J. Phys. Oceanogr.*, **41**, 657–665, https://doi.org/10.1175/2010JPO4436.1.

Kanamitsu, M., W. Ebisuzaki, J. Woollen, S. K. Yang, J. J. Hnilo, M. Fiorino, and G. L. Potter, 2002: NCEP–DOE AMIP-II Reanalysis (R-2). *Bull. Amer. Meteor. Soc.*, **83**, 1631–1644, https://doi.org/10.1175/BAMS-83-11-1631.

Kunze, E., 1985: Near-inertial wave propagation in geostrophic shear. *J. Phys. Oceanogr.*, **15**, 544–565, https://doi.org/10.1175/1520-0485(1985)015<0544:NIWPIG>2.0.CO;2.

——, E. Firing, J. M. Hummon, T. K. Chereskin, and A. M. Thurnherr, 2006: Global abyssal mixing inferred from lowered ADCP shear and CTD strain profiles. *J. Phys. Oceanogr.*, **36**, 1553–1576, https://doi.org/10.1175/JPO2926.1.

Leaman, K. D., and T. B. Sanford, 1975: Vertical energy propagation of inertial waves: Vector spectral analysis of velocity profiles. *J. Geophys. Res.*, **80**, 1975–1978, https://doi.org/10.1029/JC080i015p01975.

Lee, D. K., and P. P. Niiler, 1998: The inertial chimney: The near-inertial energy drainage from the ocean surface to the deep layer. *J. Geophys. Res.*, **103**, 7579–7591, https://doi.org/10.1029/97JC03200.

Lueck, R., 2013: Calculating the rate of dissipation of turbulent kinetic energy. Rockland Scientific International Tech. Note TN-028, 18 pp.

Mao, H., M. Feng, H. E. Phillips, and S. Lian, 2018: Mesoscale eddy characteristics in the interior subtropical southeast Indian Ocean, tracked from the Leeuwin Current system. *Deep-Sea Res. II*, **161**, 52–62, https://doi.org/10.1016/j.dsr2.2018.07.003.

McComas, C. H., and P. Muller, 1981: The dynamic balance of internal waves. *J. Phys. Oceanogr.*, **11**, 970–986, https://doi.org/10.1175/1520-0485(1981)011<0970:TDBOIW>2.0.CO;2.

McCreary, J. P., S. R. Shetye, and P. K. Kundu, 1986: Thermohaline forcing of eastern boundary currents: With application to the circulation off the west coast of Australia. *J. Mar. Res.*, **44**, 71–92, https://doi.org/10.1357/002224086788460184.

Melet, A., R. Hallberg, S. Legg, and M. Nikurashin, 2014: Sensitivity of the ocean state to lee wave–driven mixing. *J. Phys. Oceanogr.*, **44**, 900–921, https://doi.org/10.1175/JPO-D-13-072.1.

Menezes, V. V., H. E. Phillips, A. Schiller, C. M. Domingues, and N. L. Bindoff, 2013: Salinity dominance on the Indian Ocean Eastern Gyral current. *Geophys. Res. Lett.*, **40**, 5716–5721, https://doi.org/10.1002/2013GL057887.

——, ——, ——, N. L. Bindoff, C. M. Domingues, and M. L. Vianna, 2014: South Indian Countercurrent and associated fronts. *J. Geophys. Res. Oceans*, **119**, 6763–6791, https://doi.org/10.1002/2014JC010076.

Meyer, A., H. Phillips, B. Sloyan, and K. Polzin, 2014: Mixing (MX) Oceanographic Toolbox for EM-APEX float data applying shear-strain finescale parameterization. IMAS Tech. Rep. 2014/01, 77 pp., https://eprints.utas.edu.au/23309/7/Meyer_et_al_MX_library_report_2015.pdf.

——, B. M. Sloyan, K. L. Polzin, H. E. Phillips, and N. L. Bindoff, 2015: Mixing variability in the Southern Ocean. *J. Phys. Oceanogr.*, **45**, 966–987, https://doi.org/10.1175/JPO-D-14-0110.1.

Morrow, R., and F. Birol, 1998: Variability in the southeast Indian Ocean from altimetry: Forcing mechanisms for the Leeuwin Current. *J. Geophys. Res.*, **103**, 18 529–18 544, https://doi.org/10.1029/98JC00783.

——, F. X. Fang, M. Fieux, and R. Molcard, 2003: Anatomy of three warm-core Leeuwin Current eddies. *Deep-Sea Res. II*, **50**, 2229–2243, https://doi.org/10.1016/S0967-0645(03)00054-7.

——, F. Birol, D. Griffin, and J. Sudre, 2004: Divergent pathways of cyclonic and anti-cyclonic ocean eddies. *Geophys. Res. Lett.*, **31**, L24311, https://doi.org/10.1029/2004GL020974.

Munk, W., and C. Wunsch, 1998: Abyssal recipes II: Energetics of tidal and wind mixing. *Deep-Sea Res. I*, **45**, 1977–2010, https://doi.org/10.1016/S0967-0637(98)00070-3.

Nikurashin, M., and R. Ferrari, 2010: Radiation and dissipation of internal waves generated by geostrophic motions impinging on small-scale topography: Application to the Southern Ocean. *J. Phys. Oceanogr.*, **40**, 2025–2042, https://doi.org/10.1175/2010JPO4315.1.

——, and ——, 2011: Global energy conversion rate from geostrophic flows into internal lee waves in the deep ocean. *Geophys. Res. Lett.*, **38**, L08610, https://doi.org/10.1029/2011GL046576.

——, and ——, 2013: Overturning circulation driven by breaking internal waves in the deep ocean. *Geophys. Res. Lett.*, **40**, 3133–3137, https://doi.org/10.1002/grl.50542.

Nycander, J., 2005: Generation of internal waves in the deep ocean by tides. *J. Geophys. Res.*, **110**, C10028, https://doi.org/10.1029/2004JC002487.

Oakey, N., and J. Elliott, 1982: Dissipation within the surface mixed layer. *J. Phys. Oceanogr.*, **12**, 171–185, https://doi.org/10.1175/1520-0485(1982)012<0171:DWTSML>2.0.CO;2.

Osborn, T., 1980: Estimates of the local rate of vertical diffusion from dissipation measurements. *J. Phys. Oceanogr.*, **10**, 83–89, https://doi.org/10.1175/1520-0485(1980)010<0083:EOTLRO>2.0.CO;2.

Palastanga, V., P. J. van Leeuwen, M. W. Schouten, and W. P. M. de Ruijter, 2007: Flow structure and variability in the subtropical Indian ocean: Instability of the South Indian Ocean Countercurrent. *J. Geophys. Res.*, **112**, C01001, https://doi.org/10.1029/2005JC003395.

Phillips, H. E., and N. L. Bindoff, 2014: On the nonequivalent barotropic structure of the Antarctic Circumpolar Current: An observational perspective. *J. Geophys. Res. Oceans*, **119**, 5221–5243, https://doi.org/10.1002/2013JC009516.

Pollard, R. T., and R. Millard, 1970: Comparison between observed and simulated wind-generated inertial oscillations. *Deep-Sea Res. Oceanogr. Abstr.*, **17**, 813–821, https://doi.org/10.1016/0011-7471(70)90043-4

Polzin, K. L., 2008: Mesoscale eddy–internal wave coupling. Part I: Symmetry, wave capture, and results from the Mid-Ocean Dynamics Experiment. *J. Phys. Oceanogr.*, **38**, 2556–2574, https://doi.org/10.1175/2008JPO3666.1.

——, J. M. Toole, and R. W. Schmitt, 1995: Finescale parameterizations of turbulent dissipation. *J. Phys. Oceanogr.*, **25**, 306–328, https://doi.org/10.1175/1520-0485(1995)025<0306:FPOTD>2.0.CO;2.

——, E. Kunze, J. Hummon, and E. Firing, 2002: The finescale response of lowered ADCP velocity profiles. *J. Atmos. Oceanic Technol.*, **19**, 205–224, https://doi.org/10.1175/1520-0426(2002)019<0205:TFROLA>2.0.CO;2.

——, A. C. N. Garabato, T. N. Huussen, B. M. Sloyan, and S. Waterman, 2014: Finescale parameterizations of turbulent dissipation. *J. Geophys. Res. Oceans*, **119**, 1383–1419, https://doi.org/10.1002/2013JC008979.

Rennie, S. J., C. P. Pattiaratchi, and R. D. McCauley, 2007: Eddy formation through the interaction between the Leeuwin Current, Leeuwin Undercurrent and topography. *Deep-Sea Res. II*, **54**, 818–836, https://doi.org/10.1016/j.dsr2.2007.02.005.

Richardson, P. L., C. Maillard, and T. Stanford, 1979: The physical structure and life history of cyclonic Gulf Stream ring Allen. *J. Geophys. Res.*, **84**, 7727–7741, https://doi.org/10.1029/JC084iC12p07727.

Sallée, J.-B., N. Wienders, K. Speer, and R. Morrow, 2006: Formation of subantarctic mode water in the southeastern Indian Ocean. *Ocean Dyn.*, **56**, 525–542, https://doi.org/10.1007/s10236-005-0054-x.

Sanford, T. B., 1971: Motionally induced electric and magnetic fields in the sea. *J. Geophys. Res.*, **76**, 3476–3492, https://doi.org/10.1029/JC076i015p03476.

——, 1984: Circulation and internal waves in a cold Gulf Stream waves. Office of Naval Research Tech. Rep., 22 pp., https://apps.dtic.mil/sti/pdfs/ADA149704.pdf.

——, R. G. Drever, and J. H. Dunlap, 1978: Velocity profiler based on principles of geomagnetic induction. *Deep-Sea Res.*, **25**, 183–210, https://doi.org/10.1016/0146-6291(78)90006-1.

——, J. H. Dunlap, J. A. Carlson, D. C. Webb, and J. B. Girton, 2005: Autonomous velocity and density profiler: EM-APEX. *Proc. IEEE/OES Eighth Working Conf. on Current Measurement Technology*, Southampton, United Kingdom, IEEE, 152–156.

Shang, X., Y. Qi, G. Chen, C. Liang, R. G. Lueck, B. Prairie, and H. Li, 2017: An expendable microstructure profiler for deep ocean measurements. *J. Atmos. Oceanic Technol.*, **34**, 153–165, https://doi.org/10.1175/JTECH-D-16-0083.1.

Sheen, K. L., and Coauthors, 2013: Rates and mechanisms of turbulent dissipation and mixing in the Southern Ocean: Results from the Diapycnal and Isopycnal Mixing Experiment in the Southern Ocean (DIMES). *J. Geophys. Res. Oceans*, **118**, 2774–2792, https://doi.org/10.1002/jgrc.20217.

——, J. A. Brearley, A. C. N. Garabato, D. A. Smeed, L. St. Laurent, M. P. Meredith, A. M. Thurnherr, and S. N. Waterman, 2015: Modification of turbulent dissipation rates by a deep Southern Ocean eddy. *Geophys. Res. Lett.*, **42**, 3450–3457, https://doi.org/10.1002/2015GL063216.

Shriver, J. F., J. G. Richman, and B. K. Arbic, 2014: How stationary are the internal tides in a high-resolution global ocean circulation model? *J. Geophys. Res. Oceans*, **119**, 2769–2787, https://doi.org/10.1002/2013JC009423.

Siedler, G., M. Rouault, and J. R. E. Lutjeharms, 2006: Structure and origin of the subtropical South Indian Ocean Countercurrent. *Geophys. Res. Lett.*, **33**, L24609, https://doi.org/10.1029/2006GL027399.

Silverthorne, K. E., and J. M. Toole, 2009: Seasonal kinetic energy variability of near-inertial motions. *J. Phys. Oceanogr.*, **39**, 1035–1049, https://doi.org/10.1175/2008JPO3920.1.

Sloyan, B. M., 2005: Spatial variability of mixing in the Southern Ocean. *Geophys. Res. Lett.*, **32**, L18603, https://doi.org/10.1029/2005GL023568.

——, 2006: Antarctic bottom and lower circumpolar deep water circulation in the eastern Indian Ocean. *J. Geophys. Res.*, **111**, C02006, https://doi.org/10.1029/2005JC003011.

——, L. D. Talley, T. K. Chereskin, R. Fine, and J. Holte, 2010: Antarctic Intermediate Water and Subantarctic Mode Water formation in the southeast Pacific: The role of turbulent mixing. *J. Phys. Oceanogr.*, **40**, 1558–1574, https://doi.org/10.1175/2010JPO4114.1.

St. Laurent, L., A. C. Naveira Garabato, J. R. Ledwell, A. M. Thurnherr, J. M. Toole, and A. J. Watson, 2012: Turbulence and diapycnal mixing in Drake Passage. *J. Phys. Oceanogr.*, **42**, 2143–2152, https://doi.org/10.1175/JPO-D-12-027.1.

Stramma, L., and J. R. Lutjeharms, 1997: The flow field of the subtropical gyre of the south Indian Ocean. *J. Geophys. Res.*, **102**, 5513–5530, https://doi.org/10.1029/96JC03455.

Talley, L. D., 2011: *Descriptive Physical Oceanography: An Introduction*. Academic Press, 564 pp.

Thompson, R. O. R. Y., 1987: Continental-shelf-scale model of the Leeuwin Current. *J. Mar. Res.*, **45**, 813–827, https://doi.org/10.1357/002224087788327190.

——, and R. J. Edwards, 1981: Mixing and water-mass formation in the Australian subantarctic. *J. Phys. Oceanogr.*, **11**, 1399–1406, https://doi.org/10.1175/1520-0485(1981)011<1399:MAWMFI>2.0.CO;2.

Toole, J. M., and B. A. Warren, 1993: A hydrographic section across the subtropical south Indian Ocean. *Deep-Sea Res. I*, **40**, 1973–2019, https://doi.org/10.1016/0967-0637(93)90042-2.

Warren, B. A., 1981: Transindian hydrographic section at Lat. 18°S: Property distributions and circulation in the south Indian Ocean. *Deep-Sea Res.*, **28A**, 759–788, https://doi.org/10.1016/S0198-0149(81)80001-5.

Waterhouse, A. F., and Coauthors, 2014: Global patterns of diapycnal mixing from measurements of the turbulent dissipation rate. *J. Phys. Oceanogr.*, **44**, 1854–1872, https://doi.org/10.1175/JPO-D-13-0104.1.

Waterman, S., A. C. N. Garabato, and K. L. Polzin, 2013: Internal waves and turbulence in the Antarctic Circumpolar Current. *J. Phys. Oceanogr.*, **43**, 259–282, https://doi.org/10.1175/JPO-D-11-0194.1.

Whalen, C. B., L. D. Talley, and J. A. MacKinnon, 2012: Spatial and temporal variability of global ocean mixing inferred from Argo profiles. *Geophys. Res. Lett.*, **39**, L18612, https://doi.org/10.1029/2012GL053196.

——, J. A. MacKinnon, L. D. Talley, and A. F. Waterhouse, 2015: Estimating the mean diapycnal mixing using a finescale strain parameterization. *J. Phys. Oceanogr.*, **45**, 1174–1188, https://doi.org/10.1175/JPO-D-14-0167.1.

——, ——, and ——, 2018: Large-scale impacts of the mesoscale environment on mixing from wind-driven internal waves. *Nat. Geosci.*, **11**, 842–847, https://doi.org/10.1038/s41561-018-0213-6.

Wijesekera, H., L. Padman, T. Dillon, M. Levine, C. Paulson, and R. Pinkel, 1993: The application of internal-wave dissipation models to a region of strong mixing. *J. Phys. Oceanogr.*, **23**, 269–286, https://doi.org/10.1175/1520-0485(1993)023<0269:TAOIWD>2.0.CO;2.

Woo, M., and C. Pattiaratchi, 2008: Hydrography and water masses off the western Australian coast. *Deep-Sea Res. I*, **55**, 1090–1104, https://doi.org/10.1016/j.dsr.2008.05.005.

Wunsch, C., and R. Ferrari, 2004: Vertical mixing, energy and the general circulation of the oceans. *Annu. Rev. Fluid Mech.*, **36**, 281–314, https://doi.org/10.1146/annurev.fluid.36.050802.122121.